Nano Today 29 (2019) 100799

Contents lists available at ScienceDirect

Nano Today

journal homepage: www.elsevier.com/locate/nanotoday

Review

Three dimensional nanosuperstructures made of two-dimensional materials by design: Synthesis, properties, and applications

Weigu Li [a], Yun Huang [b], Yifei Liu [b], Marshall C. Tekell [c], Donglei (Emma) Fan [a,b,*]

[a] Department of Mechanical Engineering, The University of Texas at Austin, Austin, TX 78712, USA
[b] Materials Science and Engineering Program, Texas Materials Institute, The University of Texas at Austin, Austin, TX 78712, USA
[c] Department of Chemical Engineering, The University of Texas at Austin, Austin, TX 78712, USA

ARTICLE INFO

Article history:
Received 29 May 2019
Received in revised form 3 September 2019
Accepted 30 September 2019
Available online 22 November 2019

Keywords:
3D superstructures
2D materials
Graphene
Boron nitride
TMD
MXene

ABSTRACT

The recent search for advanced materials with desired properties for next-generation flexible energy and electronic devices has focused on the unique class of two-dimensional (2D) materials made of layered crystalline structures. In particular, intensive interest has been devoted to configuring 2D materials into three-dimensional (3D) nanoporous superstructures (3DSs), which can effectively prevent aggregative restacking and maximize the exposure of active nanoscale planar surfaces. Here, we survey the recent progress of 3DSs made of several important 2D materials, including graphene, boron nitride (BN), transition metal dichalcogenide (TMD), and transition metal carbide/carbonitride (MXene). The characteristics of the formed 3DSs, including density, porosity, electrochemical activity, electronic and surface properties, depend on respective synthesis approaches and conditions. The obtained 3DSs, exhibiting distinctive properties, have been exploited in an array of applications, including shielding electromagnetic, thermal, and acoustic energies; sensing chemical, optical, and mechanical signals; serving as 3D scaffolds of energy and environment devices; and supporting 3D growth of live cells and tissues. At the end, this comprehensive review is summarized with future outlooks, including the great potentials, challenges, and bottleneck issues in fabrication and large-scale implementation of 3DSs.

Contents

* Corresponding author at: Department of Mechanical Engineering, The University of Texas at Austin, Austin, TX 78712, USA.
E-mail address: dfan@austin.utexas.edu (D. Fan).

https://doi.org/10.1016/j.nantod.2019.100799
1748-0132/

Introduction

Since the discovery of 2D graphene in 2004 [1], its grand potentials have attracted immense attention in multiple fields, including electrochemistry, electronics, biomedical and environmental engineering [2]. The unique properties and promising applications of graphene have also triggered the intensive interests and studies of various non-graphene 2D materials, such as BN [3], graphitic carbon nitride (g-CN) [4], TMD [5], MXene [6], and black phosphorus (BP) [7]. Those 2D materials consist of a single layer or few layers of covalently bonded atomic sheets interacted by van der Waals forces. The broad spectrum of 2D materials delivers a wide range of properties, ranging from electrical/thermal conductors to insulators. However, the serious restacking and aggregation of such 2D materials have hindered the full manifestation of their exceptional electrical and chemical properties. The additional processes necessary to separate 2D materials from liquid suspensions in certain applications, such as water purification, also limit the applicability and practicability. Therefore, it is desirable to synthesize 2D materials into free-standing 3D superstructures with controllable hierarchical porosity with enhanced physical and chemical properties [8,9].

In particular, the assembly of 2D materials into 3D structures not only circumvents undesirable restacking and, thus, preserves the unique characteristics of 2D materials, but also provides additional advantages, such as large accessible surface area, mechanical durability, and feasibility of being utilized as substrate-free components in macroscopic devices. The resulting 3D architectures have demonstrated tremendous potencies in numerous applications [8,10–15], including energy conversion [16,17], storage [18,19], and dissipation [20–22], sensing [23], water treatment [24], and tissue engineering platforms [25]. Commonly referred to as foams, networks, woven fabrics, aerogels, hydrogels, sponges, frameworks, monoliths, and papers, 3DSs have emerged with various synthesis methods. They can be generally categorized into either high temperature and gas involved chemical vapor deposition (CVD) and thermolysis, and solution based self-assembly, or template-assisted and template-free synthesis.

To date, there have been numerous insightful review papers on 3DSs made of 2D materials, but most of them primarily cover graphene and graphene derivatives with very little focus on non-graphene 2D materials [8,13,15,26–29]. This work summarizes the structures and properties of 3D graphene, BN, TMD, and MXene, and the state-of-art synthesis approaches of constructing those 3DSs with tailored structures for a broad spectrum of applications. Given that solution synthesis of 3D graphene has been intensively reviewed by many other great articles [9,30,31], this review primarily discusses the CVD growth of graphene foams (GF) and the relationship between the employed templates, gas precursors, deposition conditions and the resulting porosity, chemistry, lattice structures, morphologies, and electrical properties. In contrast to 3D graphene, the fabrication of 3D BN, TMD, MXene can be mainly achieved by solution-based self-assembly methods, such as dip coating, freeze-drying, filtration, hydrothermal reaction, and

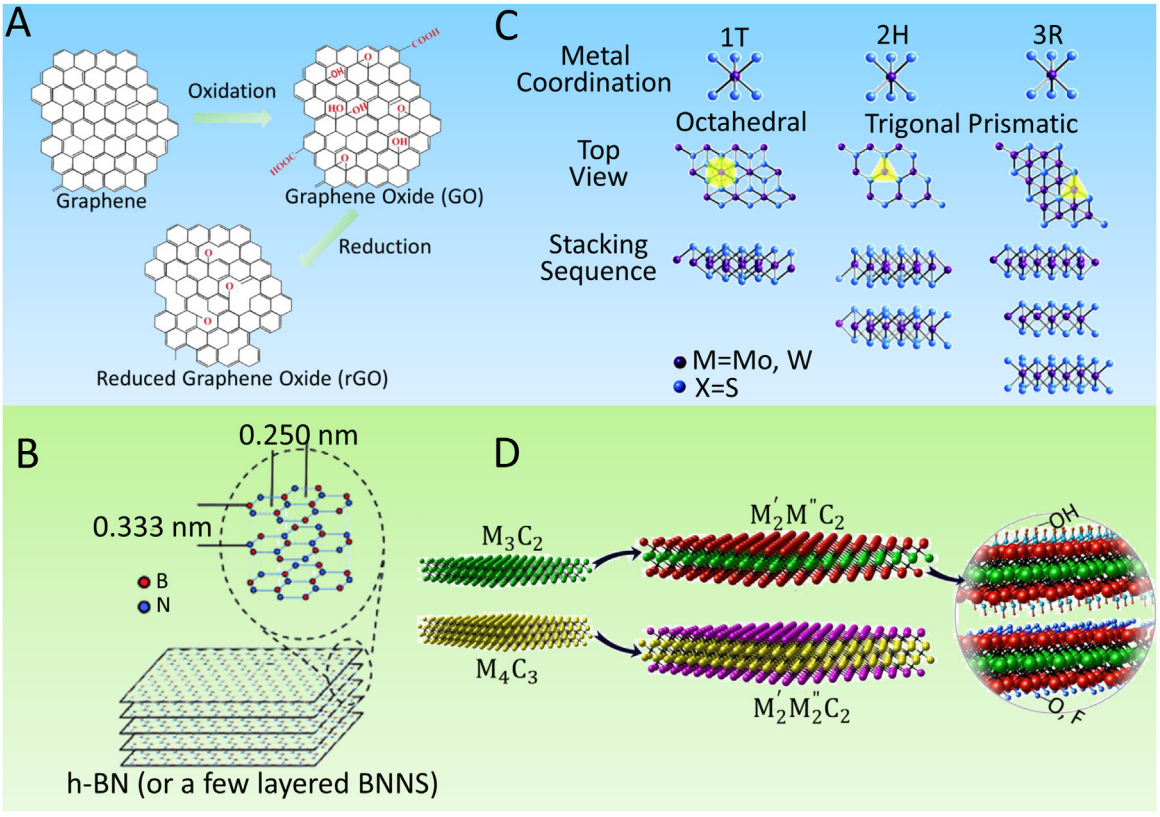

Fig. 1. Structures of various 2D materials. (A) Chemical structures of graphene, GO, and rGO [32]. (B) Atomic structures of few-layer h-BN [46]. (C) Metal coordination and stacking sequence of TMD structural unit cells [50]. (D) Structures of 2D MXenes [53]: schematics of conventional single transition metal MXenes, and double transition metal MXenes $M'_2M''C_2$ and $M'_2M''_2C_3$ (M' and M'' are different elements: Ti, V, Nb, Ta, Cr, or Mo).
(A) Reproduced with permission from Ref. [32]. Copyright 2018, Springer Berlin Heidelberg, is licensed under CC BY 4.0. (B) Reproduced with permission from Ref. [46]. Copyright 2012, Royal Society of Chemistry. (C) Reproduced with permission from Ref. [50]. Copyright 2017, Royal Society of Chemistry, is licensed under CC BY 3.0. (D) Reproduced with permission from Ref. [53]. Copyright 2015, American Chemical Society.

cross-linking, which are all featured in this work. Furthermore, we systematically review the application-oriented structural design and hybridization of 2D materials with active guest materials. The applications include energy conversion and storage; shielding electromagnetic waves, heat, and acoustic energy; biochemical, optical, and mechanical sensing; and porous scaffolds for cell culturing. The review is concluded with prospects, challenges, and opportunities.

Structures and properties of 2D materials

Graphene

Graphene is a one-atom-thick 2D layer of honeycomb lattice consisting of sp^2–bonded carbon atoms [Fig. 1A] [32]. The unique structure imparts graphene supreme materials properties, such as ultrahigh room-temperature electron mobility ($2.5 \times 10^5\ cm^2\ V^{-1}\ s^{-1}$) [33] and thermal conductivity ($5150\ W\ m^{-1}\ K^{-1}$) [34], excellent mechanical stiffness (Young's modulus: 1 TPa; intrinsic strength: 130 GPa) [35], exceptionally large specific surface area ($2630\ m^2\ g^{-1}$) [36], and superior optical transmittance (97.7%) [37]. Single-layer or several-layer graphene nanosheets can be obtained by mechanical exfoliation [38], liquid exfoliation [39], and CVD [40–42]. Graphene oxide (GO) [Fig. 1A], a kind of chemically modified graphene prepared by oxidation and exfoliation is also regarded as a 2D material of the graphene family, which is a monolayer structure with a high oxygen content, typically characterized by C/O atomic ratio less than 3.0 [43,44]. After reduction with chemical or thermal methods, GO can be converted to reduced graphene oxide (rGO) [Fig. 1A] [43].

Boron nitride

Boron nitride (BN), an analog to graphite both in electronic number and crystal structure, exists in three major polymorphs, hexagonal boron nitride (h-BN), sphalerite boron nitride (β-BN) and wurtzite boron nitride (ɣ-BN), among which h-BN is the most stable type [45]. Unless otherwise specified, the BN in this paper refers to h-BN. BN possesses thermal conductivity and mechanical properties comparable to graphite. However, due to the polarity of B—N bonds, the symmetry of electron states of BN is broken and an intrinsic bandgap of 5.9 eV is developed, making BN an electrical insulator. Similar to graphene, boron and nitrogen atoms interact with each other with covalent bonds within one single layer and stack with van der Waals interactions [Fig. 1B] [46]. Single- to few-layer BN shows an average Young's modulus of 0.865 TPa and fracture strength of 70.5 GPa [47]. The theoretical thermal conductivity of monolayer BN, which can be as high as $1700–2000\ W\ m^{-1}\ K^{-1}$, is among the best of the thermal conductive materials discovered so far [48]. Furthermore, BN is stable in corrosive environments and at temperatures over 800 °C in air, indicating its superior chemical inertness and thermal stability [49].

Transition-metal dichalcogenide

Transition metal dichalcogenide (TMD) refers to a class of atomically thin semiconductor materials with a chemical formula of MX_2, where M stands for the transition metal atom (Mo, W, Co, Ni, etc.), and X for the chalcogen atom (S, Se, or Te). Similar to graphite, bulk

TMD crystals are made of monolayer stacks assembled by van der Waals force. In each single layer, two layers of chalcogen atoms sandwich one layer of metal atoms via covalent bonds. Most bulk TMDs have three polymorphs: trigonal (1 T), hexagonal (2 H) and rhombohedral (3R) phases, which are distinguished by the stacking sequence. Among them, the 2H phase is the most stable one. The schematic image of the crystal structures of TMD is shown in Fig. 1C [50]. Due to their layered structure and relatively large interlayer distance (~0.6 nm) compared to graphite (~0.335 nm), lithium ions can readily intercalate into bulk TMDs. The physical properties of TMDs can vary from insulating, semiconducting to metallic, as represented by HfS_2, MoS_2, and $NbSe_2$, respectively [51]. Most semiconductor TMDs also exhibit thickness-dependent bandgaps. For instance, the bandgap of MoS_2 changes from 1.2 eV (bulk) to 1.9 eV (monolayer), accompanied with a transition from indirect to direct bandgap structure [52].

MXene

MXene is a group of emerging 2D materials composed of transition metal carbides, carbonitrides and nitrides with the general formula of $M_{n+1}X_nT_X$, where M is an early transition metal, such as Sc, Ti, V, and Cr, X represents carbon or nitrogen and T_X refers to surface termination molecules, such as —OH, —O or —F groups [Fig. 1D] [53]. One MXene sheet usually consists of 3, 5, or 7 atomic layers, corresponding to M_2X, M_3X_2, or M_4X_3, respectively. There would be 2 more layers if the aforementioned functional termination groups are presented and bonded to the outer transition metal layers. The termination layers are the common results from the synthesis in acidic fluoride-containing solution. Apart from single metal carbides, such as Ti_3C_2 and Ti_4C_3, compounds with binary metals also exist, including Mo_2TiC_2, $Mo_2Ti_2C_3$. Because of their metallic conductivity (9880 S cm^{-1}) [54], high Li storage capacity (447.8 mA h g^{-1}) [55], ultrahigh theoretical capacitance (1982 F cm^{-3}) [56] and hydrophilic surfaces, MXene is generally viewed as promising materials for electrochemical energy conversion and storage devices.

CVD synthesis of 3D superstructures

The methods of constructing 2D materials into 3DSs are pivotal to the structures and properties of 3D architectures and, hence, are of paramount significance for the respective applications. In this review, the synthesis techniques are classified into high-temperature and gas involved CVD (including thermolysis) and solution based self-assembly. The self-assembly method that creates 3DSs from colloids of exfoliated 2D materials is commonly cost-effective, high-yield, and amenable to large-scale manufacturing. However, the self-assembly approach commonly induces defects in the lattice structure of 2D materials that impair the captivating electrical properties. In contrast, 3DSs synthesized via CVD technique exhibit better crystallinity and electrical properties with controllable porosity. However, the employed high temperature increases the cost and requires the maintenance of the equipment.

Chemical vapor deposition is a process whereby a solid material is deposited from the vapor phase by the decomposition of chemicals occurring on the surface of a heated substrate surface. Thermolysis is a process of thermal decomposition of materials at elevated temperature in an inert atmosphere. If the decomposed materials are organics, the process is also referred as to pyrolysis. Since both processes involve the employment of high temperature and gases, this review generalizes them as one section.

CVD synthesis of 3D graphene

Conventional CVD synthesis of 3D graphene

The CVD synthesis of 3D graphene usually involves the use of catalytic templates that facilitate the decomposition of the carbon source (CH_4, CH_3CH_2OH, C_2H_4, C_2H_2, and C_6H_6) for deposition of graphene and that can be removed after CVD to obtain free-standing ultralight 3D GF. The catalytic templates can be 3D metallic scaffolds (e.g. Cu meshes [57,58], and Ni foams [59,60]) or porous metal oxides (e.g. Al_2O_3 [61,62], and CaO [63]).

Since the solubility of carbon in Cu is much lower than that in Ni, the CVD growth of graphene on Cu is proposed as a surface adsorption process [42,64], whereas the synthesis of graphene on Ni is regarded as carbon segregation and precipitation [64,65]. Therefore, CVD growth on Cu substrates usually results in monolayer graphene that is difficult to be self-supported in 3D macrostructures [44,64]. In contrast, multilayer growth of graphene on nickel substrates is feasible and the 3D growth of graphene on nickel foams is more widely adopted [8,44]. In 2011, Cheng group reported the first CVD fabrication of 3D GF using commercial Ni foams as catalytic templates and methane as a carbon source at a high temperature of 1000 °C as illustrated in Fig. 2A [59]. The catalytic templates can be strategically tailored and selected to tune the size, shape, density, distribution of pores in the 3D graphene foams. The selected carbon source and modified CVD technique also influence the morphology, quality and physicochemical properties of synthesized graphene foams.

CVD synthesis with strategically engineered catalytic templates

Though commercial Ni foams are excellent templates for 3D CVD growth of graphene, the large pore size of a few hundred micrometers limits the applications. To enhance the surface area, one needs to fully utilize the empty spaces between the interconnected Ni micro-struts. Fan group created multilevel porous nickel foams with second level micropores of 1.9–8.3 μm on the main branches [18,66,67] and ramified porous nickel foams with Cu-Ni alloy microdendrites filling in the empty interspace of nickel branches [Fig. 2B] [19] through electrochemical subtractive and additive manufacturing on commercial nickel foams. Such microstructures result in graphene foams with up to a three-fold enhancement in surface area. Besides the strategically engineered commercial nickel foams, other research groups also created novel porous nickel templates with customized porosity, such as nanoporous Ni substrates made by electrochemically leaching Mn from cold-rolled $Ni_{30}Mn_{70}$ sheets in acid [Fig. 2C] [68], 3D porous nano-Ni film prepared via electrodeposition with a dynamic hydrogen bubble template [69], and microcellular Ni foams fabricated by electroless plating of Ni films on sintered poly(methyl methacrylate) (PMMA) spheres [70]. Moreover, GF can be also synthesized using templates made of pressed and/or sintered nickel nanowires [71], powders or pellets [Fig. 2D] [72–77]. These nickel materials are either chemically synthesized [71,77], or commercially available [72–76]. Graphene foams fabricated through those strategically engineered catalytic templates usually deliver enhanced surface area, porosity, and reduced mass density.

Porous oxide templates are also exploited for metal-catalyst-free CVD growth of 3D GF, including porous MgO [78], anodic aluminum oxide (AAO) templates and porous Al_2O_3 ceramic substrates [62], AAO wires [61], and calcined seashells (porous CaO) [63]. It is proposed that oxygen atoms on the surface of templates are beneficial to the direct nucleation and growth of graphene as they enhance the absorption and decomposition of hydrocarbons at high temperature and, thus, promote the carbon-carbon coupling on the substrates [63,79,80]. Liu group developed a microporous

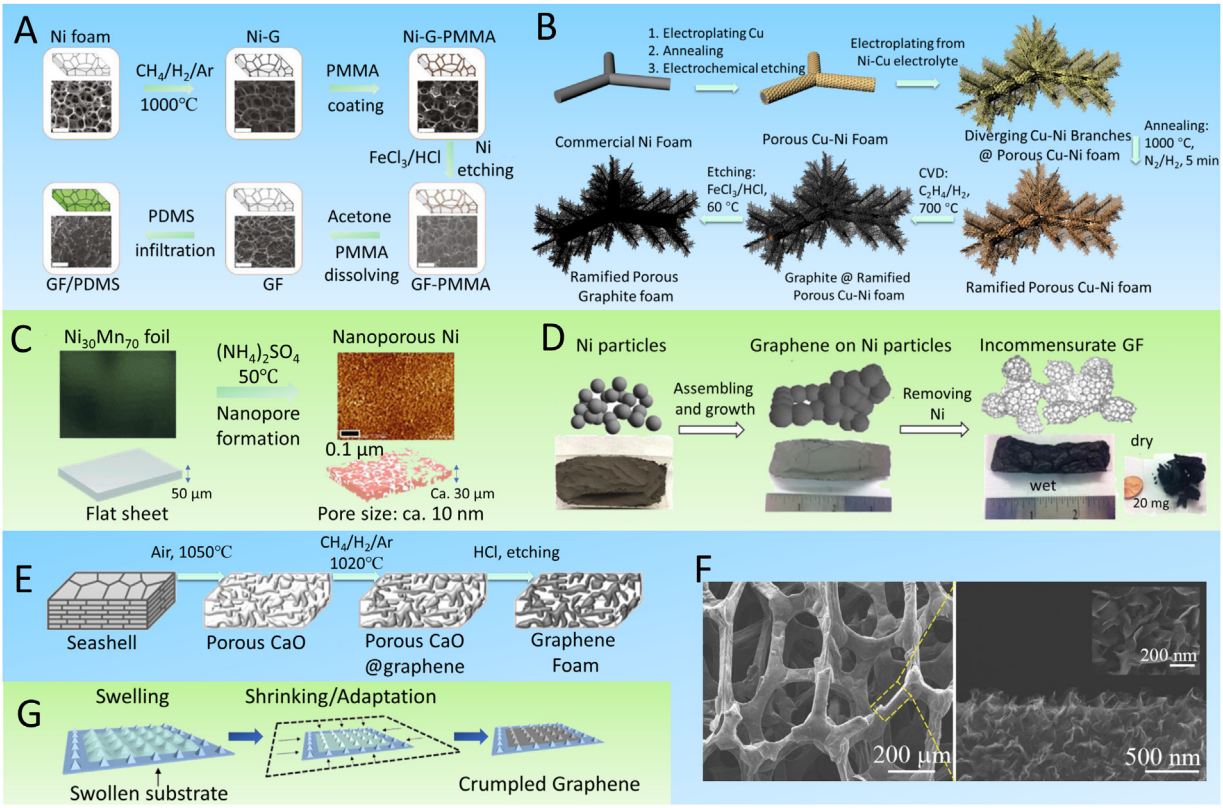

Fig. 2. CVD growth of 3D GF with a variety of templates: (A) commercial Ni foams [59]; (B) ramified porous Ni foams [19]; (C) nanoporous Ni foams [68]; (D) closed-packed Ni powders [74]; (E) porous CaO (calcined seashell) [63]. (F) SEM images of hierarchical GF with vertical graphene nanosheets on graphitic struts [90]. (G) Fabrication of crumpled graphene on a swollen PDMS substrate [97].
(A) Reproduced with permission from Ref. [59]. Copyright 2011, Springer Nature. (B) Reproduced with permission from Ref. [19]. Copyright 2018, John Wiley and Sons. (C) Reproduced with permission from Ref. [68]. Copyright 2014, John Wiley and Sons. (D) Reproduced with permission from Ref. [74]. Copyright 2017, Springer Nature, is licensed under CC BY 4.0. (E) Reproduced with permission from Ref. [63]. Copyright 2016, American Chemical Society. (F) Reproduced with permission from Ref. [90]. Copyright 2017, John Wiley and Sons. (G) Reproduced with permission from Ref [97]. Copyright 2015, American Chemical Society.

CaO template by calcinating scallop seashells and grew GFs with an extremely low density of ~3 mg cm^{-3} [Fig. 2E] [63].

Carbon source of CVD synthesis

The carbon source involved in CVD synthesis of 3D GF is usually methane, ethanol, acetylene, or benzene at a high temperature of 900–1000 °C. Some researchers choose to use ethylene (C_2H_4) instead of methane because the high reactivity of C_2H_4 allows graphene to grow at a deposition temperature as low as 700 °C [18,66,67]. It is found that low-temperature growth leads to thicker graphene layers (>10 layers) but with more defects [81,82]. The multilayer GFs are usually called as ultrathin graphite foams, which are better free-standing and self-supported than single- or few-layer GFs [18,66,67]. Because of their improved mechanical properties, PMMA is not needed as a support during the etching process.

The use of carbon sources other than pure hydrocarbons allows one to grow graphene doped with other elements such as nitrogen (N), boron (B) and sulfur (S). Nitrogen can be doped into the hexagonal graphene lattice by using ethylenediamine [17], pyridine [83,84], or a mixture of hydrocarbon gas and NH_3 [17]. Boron-doped graphene can be obtained by using toluene and triethyl borate as carbon and boron sources [17]. The co-doping of N and B [17], or N and S [82], can be realized by utilizing melamine diborate [17], or pyridine and thiophene as CVD precursors [82], respectively. Doping in GFs can enrich free charge-carrier density and enhance electrical conductivity [85,86], augment lattice defects and provide more active sites for electrochemical applications [17,82,87], reduce thermal conductivity [83], and improve hydrophilicity [83].

PECVD synthesis of 3D graphene

Vertical graphene nanosheets can be grown on either metal or metal-free substrates through microwave plasma-enhanced CVD (PECVD) [88]. This modified CVD technique can be also adopted for the growth of hierarchical GF (h-GF) foams [Fig. 2F] [89–91]. GFs containing such vertical graphene sheets exhibit multiple advantages: (1) they can fully expose the chemically active graphene edges and enable facile electrolyte access [89,91]; (2) they provide enlarged surface area either for electrochemical reactions or heat exchanges [90,91]; (3) the vertical nanostructures guarantee the optical absorption at an arbitrary incident angle with decreased light reflection [90].

Wrinkling engineering for crumpled graphene

Two-dimensional sheets of CVD-grown graphene can be "crumpled" into 3D structures. Although some wrinkling of 2D materials during synthesis, handling, and subsequent processing is inevitable, introducing controlled topographical features to the CVD-prepared graphene requires treatment either pre- or post-deposition. Three major approaches have been developed to achieve scalable crumpling [92]. First, the CVD-prepared graphene can self-shrink into crumpled graphene on an ethanol solution surface owing to the reduced surface and interface energy of the graphene/ethanol system [93]. Second, by designing the surface morphology of the CVD growth template, crumpled graphene with tunable wrinkling dimension, density and orientation can be obtained [94]. Third, transferring the CVD-grown graphene onto engineered foreign substrates, such as pre-stretched [95,96] and

swollen [Fig. 2G] [97] surfaces, also results in the formation of crumpled graphene.

CVD synthesis of 3DSs made of beyond-graphene 2D materials

Similar to graphene, 2D sheets of BN and TMDs can be also incorporated into 3DSs via CVD; the CVD synthesis of 3D MXene, however, has yet to be reported. In contrast to metallic templates for CVD-grown GF, CVD substrates employed for 3DSs of BN and TMDs only serve as sacrificial or supporting scaffolds and have no catalytic function. The CVD substrates can be nickel foams [98–100], aerogels [101–103], and polymer sponges [104]. The involved gas precursors vary from the category of 2D materials.

CVD synthesis of 3D BN

Golberg group fabricated 3D tubular BN networks with SiO_2 aerogel as an initial template as illustrated in Fig. 3A [103]. N-doped graphitic/SiO_2 foam was firstly synthesized via an *N*, *N*-dimethylformamide (DMF) assisted CVD. Then, 3D BN foam can be synthesized via a modified carbothermal-reduction CVD reaction in the presence of B_2O_3 and nitrogen vapor. Here, the doped nitrogen atoms provide sites for the B_2O_3 vapor to be adsorbed and further converted to continuous BN. As a result, BN networks with pore sizes ~0.36 μm were synthesized [103]. Guo group synthesized porous BN using nickel foam as the template by low-temperature CVD [100]. Here, borazine powder was used as the precursor and a piece of nickel foam was used as the substrate. Benefiting from the large pore size and the hollow branches structure, the BN foam was ultralight with a density of 1.6 mg cm^{-3} and exhibited balanced rigidity and elasticity.

CVD synthesis of 3D TMD

Ni foams can be used as precursors for the synthesis of nickel dichalcogenides, a member of TMD that exhibits good electrical conductivity. Foams made of hybrid $NiSe_2$/Ni can be obtained by one-step selenization of Ni foam via a CVD method [99]. Based on this work, Ren group further grew ternary molybdenum sulfoselenide ($MoS_{2(1-x)}Se_{2x}$) and ternary tungsten sulfoselenide ($WS_{2(1-x)}Se_{2x}$) on the $NiSe_2$ foam via thermal selenization of surface coated $(NH_4)_2MoS_4$ [Fig. 3B] [105], and $(NH_4)_2WS_4$ [106].

Thermolysis synthesis of 3D superstructures

Apart from the use of toxic and flammable carbonaceous gas, 3D GFs can be also synthesized via thermolysis of polymer (pyrolysis) in the presence of nickel catalysts. Lee et al. reported a 3D graphene nanofoams by annealing polyvinyl alcohol (PVA)/$NiCl_2$ film in a gas mixture of H_2 and Ar at 1000 °C [107]. Nanopores (40–50 nm) were generated by the loss of organic materials during the carbonization process. Carbonized-C and reduced nickel in a 3D nanoframe created by the pyrolysis of the sample in a hydrogen gas environment provided a solid carbon source and a catalyst for the graphene growth in the CVD process, respectively. 3D graphene structures were also obtained by pyrolyzing photoresist films patterned by interference lithography [108], where 3D amorphous carbon structures were conformally sputtered with nickel and then annealed, converting the materials into 3D graphitic monoliths [Fig. 3C]. Ye group mixed and pressed melamine and Ni powders, then annealed them in a CVD furnace with H_2/Ar flowing under a negative pressure, where Ni powders served as catalysts and reaction templates while melamine decomposed into carbon and nitrogen and deposited onto the nickel surface [Fig. 3(D, E)] [75].

Similarly, BN foams can be obtained by thermolyzing the porous monolithic precursor in an ammonia atmosphere. The precursor can be obtained from self-bubbling [109] and freeze-drying [Fig. 3F] [20]. The introduced ammonia could preferably favor the conversion of B—O into B—N at high temperature, efficiently removing the C elements in the precursor and offsetting the loss of N during the thermolysis process. For instance, Golberg group prepared the precursor by self-bubbling solidification of boric acid in formaldehyde-dicyandiamide resin (FDR) solution [109]. After pyrolysis at 1000 ° for 6 hours, porous BN structure with a high specific surface area and high bulk crush strength was synthesized [109]. Large size (~23 cm) ultralight BN foams were achieved by Tang group with a similar pyrolysis process [20]. However, the bulk precursor was obtained by freeze-drying the mixture of boric acid and melamine in distilled water. The synthesized BN foam was constructed by porous BN microfibers and exhibited a high porosity of ~99.3% [20].

The pioneering work on the thermolysis synthesis of 3D TMD superstructures was reported by Li group [110]. $(NH_4)_2MoS_4$ coated on GF/Ni is was annealed in H_2/Ar environment at various temperatures (100–300 °C) and decomposed to MoS_x film on the surface. Almost at the same time, Zhang group developed a similar method to synthesize MoS_2 nanosheets on graphene foam [Fig. 3G] [111]. Inspired by their work, vertical ReS_2 nanosheets on 3D graphene foam were synthesized by using NH_4ReO_4 transition metal precursors and H_2S/Ar as the thermolysis atmosphere [112]. Unlike the randomly grown MoS_2, the vertical ReS_2 nanosheets uniformly dispersed on the graphene foam, as displayed in Figs. 3(H, I) [112]. Free-standing MoS_2 and WS_2 aerogels can be also obtained by in-situ thermolysis of their aerogel precursors as well [Fig. 3J] [113,114]. In this method, ammonium thiomolybdate (ATM) and ammonium thio-tungstate (ATT) were dissolved in deionized water and then submerged in liquid nitrogen to dry rapidly. The obtained ATM and ATT aerogels were then sealed in 2% H_2/98% inert gas at 450 °C for 4 h. After cooling to room temperature, free-standing MoS_2 and WS_2 aerogel can be obtained.

Solution based self-assembly of 3D superstructures

Solutions of GO dispersions can be arranged into 3D porous architectures through controlled self-assembly or the use of solid templates and fluid interfaces. Strategies for the solution-based synthesis of 3D porous graphene have been well researched and documented in several insightful reviews [9,30,31]. In order to avoid overlap, this review provides a general overview of the solution-based synthesis mechanism of 3D graphene, which could apply to 3DSs made of 2D materials besides graphene or graphene derivatives. Examples will be discussed in the solution-based self-assembly of 3D BN, TMD, and MXene.

Solution based self-assembly of 3DSs made of graphene oxide

Dispersing GO nanosheets in an aqueous solution creates a stable colloid that can be purposely destabilized, freeze-dried, and reduced to create 3D graphene with a variety of chemical compositions and physical morphologies. The colloidal stability of GO suspensions depends on the balance of attractive and repulsive forces between GO nanosheets. In theory, universally attractive van der Waals forces between GO sheets in solution must be counterbalanced with repulsive electrostatic forces to form a stable colloid [115]. Thus, the general scheme for the fabrication of 3D graphene involves the removal of repulsive forces and the generation of attractive forces via hydrothermal reduction [116,117]. The dynamic amphilicity of the GO nanosheets during the reduction process produces the porous structure. Supercritical water acts as a reducing agent, removing the functional groups, exposing the hydrophobic basal plane and promoting π-π stacking between adjacent basal planes. Residual functional groups, however, expe-

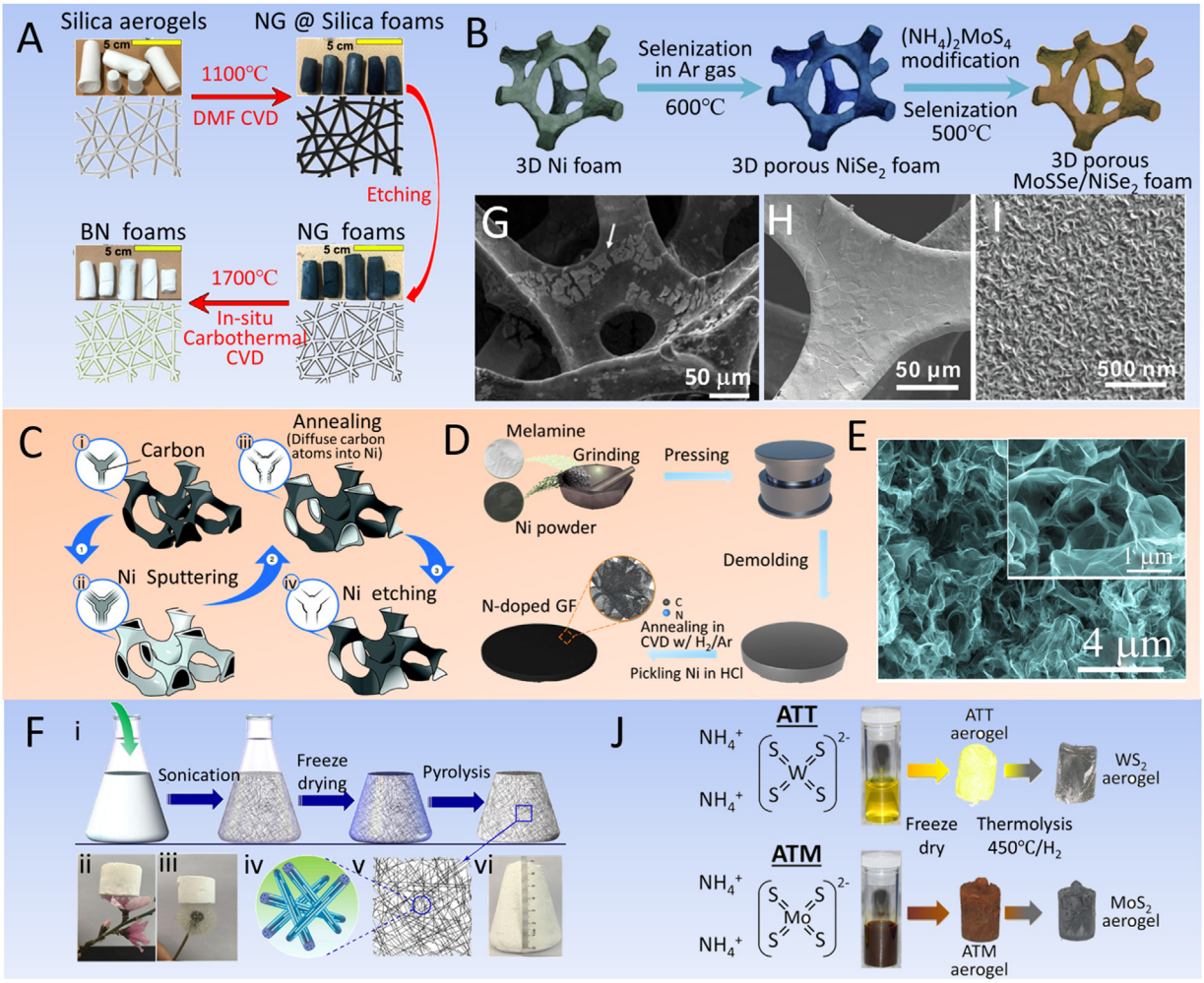

Fig. 3. CVD and thermolysis synthesis of 3DSs. (A) Schematic of CVD synthesis of 3D Tubular BN cellular Network Foams [103]. (B) Schematic of CVD growth of ternary $MoS_{2(1-x)}Se_{2x}$ particles on $NiSe_2$ foam [105]. (C) Schematic of pyrolysis of amorphous porous carbon (lithographically defined photoresist) to 3D GF [108]. (D) Schematic of the synthesis of N-doped GF using Ni powders [75]. (E) SEM images of N-doped GF in Fig. 3D [75]. (F) Pyrolysis synthesis of ultralight BN foam [20]: (i) steps of the synthesis of 3D BN foam via freeze-drying and pyrolysis; (ii, iii) the BN foam is ultralight which can be held by dandelion and petals of flowers; (iv, v) micro-network structure of the BN foam; (vi) photographs of as-prepared BN foam with a large size. (G) SEM image of the MoS_2/3DGN composite [111], the arrow points at the micro-sized MoS_2 flakes. (H, I) Vertical ReS_2 nanosheets grown on Ni foam [112]. (J) Thermolysis synthesis of WS_2 and MoS_2 aerogels [113].
(A) Reproduced with permission from Ref. [103]. Copyright 2017, American Chemical Society. (B) Reproduced with permission from Ref. [105]. Copyright 2016, Springer Nature, is licensed under CC BY 4.0. (C) Reproduced with permission from Ref. [108]. Copyright 2012, American Chemical Society. (D, E) Reproduced with permission from Ref. [75]. Copyright 2018, Elsevier. (F) Reproduced with permission from Ref. [20]. Copyright 2017, American Chemical Society. (G) Reproduced with permission from Ref. [111]. Copyright 2013, John Wiley and Sons. (H, I) Reproduced with permission from Ref. [112]. Copyright 2016, John Wiley and Sons. (J) Reproduced with permission from Ref. [113]. Copyright 2015, American Chemical Society.

rience hydrogen bonding with water and trap water in pores on the micrometer scale.

Besides hydrothermal reduction, there are various approaches of building 3DSs of GO, such as chemical reduction [118], change in pH [119], addition of crosslinkers [120], freeze-drying [121], and filtration [85,122]. In contrast to the hydrothermal method, chemically assisted reduction allows rGO hydrogels to form at much lower temperatures with shorter reaction times at atmospheric pressure. Freeze-drying prevents volume shrinkage and pore collapse that would result from drying in ambient conditions. Filtration is another facile and efficient way of separating solids from liquid with controlled thickness and high yield. Moreover, the addition of crosslinkers like PVA in the reduction process can promote the gelation of GO. Appropriate choices of chemical reductants, crosslinkers, active materials, and even other 2D materials can create 3D graphene structures with chemical dopants, optimized porosities, and functionalized surfaces. These principles will be elaborated in the review of the following self-assemblies of 3DSs made of BN, TMD, and MXene. Furthermore, recent advances in 3D printing [123], and laser-induced/scribed graphene [124] have emerged to solve issues related to optimized microscopic structure, customized macroscopic morphology, and large-scale manufacturability. In the future, these advances will likely be mirrored in the self-assembly of beyond-graphene 2D materials.

Solution based self-assembly of 3DSs made of beyond-graphene 2D materials

Hydrothermal synthesis

Distinct from the hydrothermal synthesis of 3D GO composites, the hydrothermal synthesis of 3DSs made of beyond-graphene materials usually utilizes porous structures such as nickel foams, GFs, carbon foams/cloths, and polymer sponges as templates, which are immersed in a solution of precursors and sealed in a Teflon autoclave. By controlling the concentration of the precursor, reaction temperature, and time, various kinds of 2D nanostructures can be directly synthesized on the templates. For instance, Shen group synthesized honeycomb-like MoS_2 nanoarchitectures on 3D

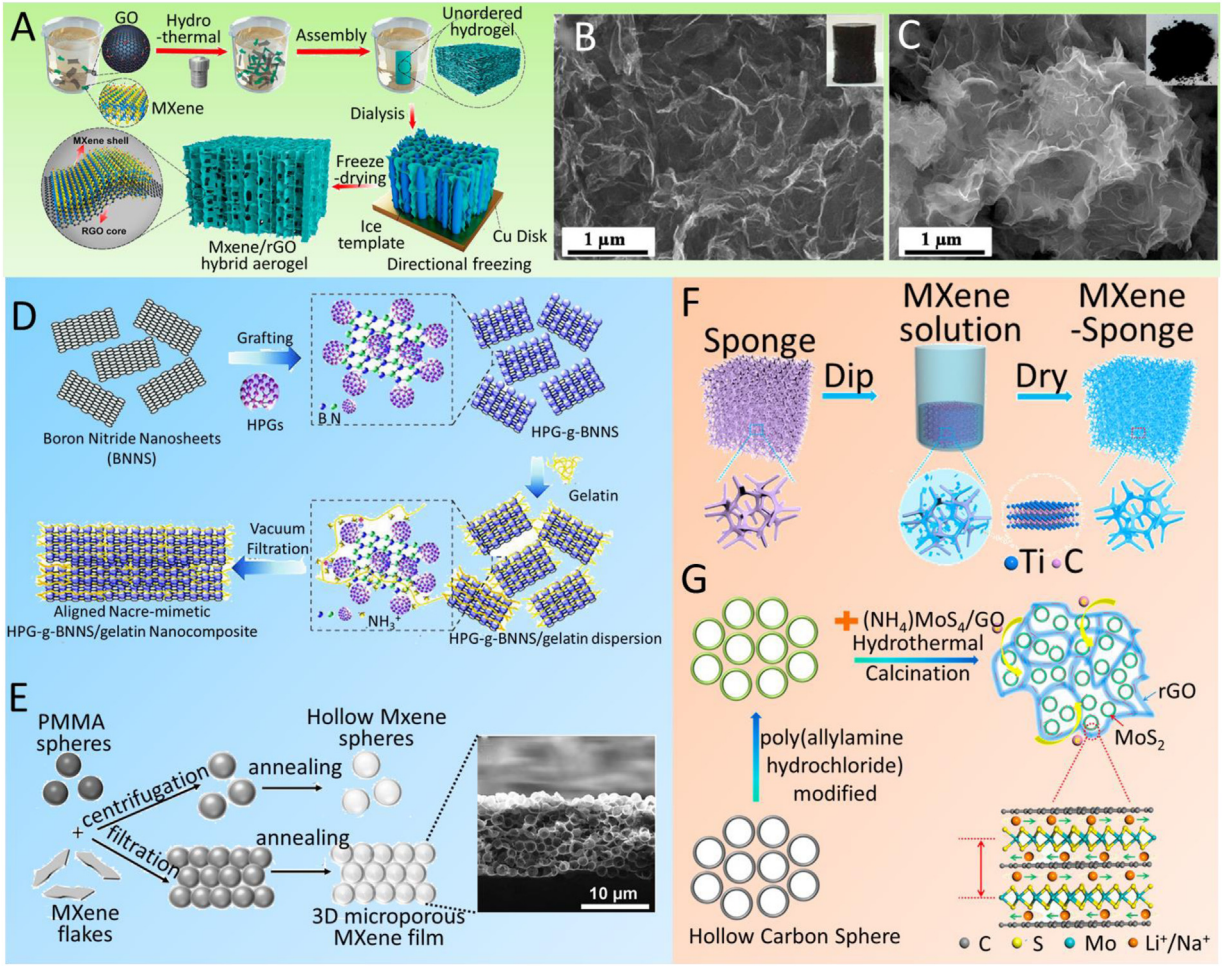

Fig. 4. Solution-based self-assemblies of 3DSs. (A) Freeze-drying synthesis of $Ti_3C_2T_X$ MXene/rGO hybrid aerogel [136]. (B, C) 3DMG aerogels [134]: SEM images of MG aerogels (B) and bare MoS_2 (C) the insets show the photographs of bare MoS_2 and MG aerogels respectively. (D) Vacuum filtration-induced self-assembly technique for the synthesis of HPG-g-BNNSs/gelatin nanocomposite [141]. (E) Filtration synthesis of 3D macroporous MXene films [142]: schematic of the construction of hollow MXene spheres and 3D macroporous MXene frameworks; the image on the right: cross-sectional SEM image of the 3D macroporous $Ti_3C_2T_X$ film. (F) Dip-drying synthesis of MXene-sponge via dipping-drying [143]. (G) Synthesis of MoS_2 on 3D networks formed by the cross-linking between HCS with rGO [151].
(A) Reproduced with permission from Ref. [136]. Copyright 2018, American Chemical Society. (B, C) Reproduced with permission from Ref. [134]. Copyright 2016, Elsevier. (D) Reproduced with permission from Ref. [141]. Copyright 2018, John Wiley and Sons. (E) Reproduced with permission from Ref. [142]. Copyright 2017, John Wiley and Sons. (F) Reproduced with permission from Ref. [143]. Copyright 2018, Elsevier. (G) Reproduced with permission from Ref. [151]. Copyright 2018, American Chemical Society.

GF (MoS_2/GF) via a hydrothermal reaction between Na_2MoO_4 and thiourea with the assistance of surfactant P123 at 200 °C for 24 h [125]. Following this work, MoS_2 nanostructures were synthesized on N-doped graphene sheets [126], graphene wrapped carbon microtubes [127] and cellulose paper [128] via hydrothermal methods [126–128]. Apart from MoS_2, 3D structures made of other TMDs, like $MoSe_2$/Ni foam [129], WS_2/Ni foam [130], FeS_2/GF [131], and VO_2/graphene@NiS_2 aerogel [132], can be synthesized as well. Though hydrothermal synthesis is a facile approach, the quality of the 3DSs is generally compromised due to the stacking of 2D materials. It is also challenging to control the final morphology of the structures. We also note that there is almost no report on the direct synthesis of 3D BN and 3D MXenes through hydrothermal synthesis because of the intrinsic fabrication limitation of 2D BN and MXene.

Freeze-drying synthesis

Freeze-drying is a powerful technique that is utilized in the synthesis of 3DSs. During the rapid cooling process, liquid water will transform into solid ice and separate from the nanoarchitectures. The porous structures can be maintained without shrinking by the following sublimation of ice. However, because of the local differences in the freezing rates and associated temperature gradients, the morphology of 3DSs is generally not uniform. A typical freeze-drying process is illustrated in Fig. 4A. A wide spectrum of 2D materials can be assembled into 3DSs through freeze-drying, such as BN/PVA hydrogel [133], MoS_2/rGO (MG) hydrogel [Fig. 4B] [134], and MXene/rGO aerogel [Fig. 4A] [135,136]. In most of freeze-drying synthesis processes, GO and the reduction of GO through hydrothermal reaction are involved because rGO nanosheets play a vital role in the formation of the interconnected porous network due to the π-π interactions and the resulting hydrophobic nature. Without rGO nanosheets, 2D nanosheets tightly clumped together during the freeze-drying process as shown in Fig. 4C [134].

Filtration

Filtration can separate solids of 2D materials from the liquid phase and form a thin-film 3D monolithic structure. It shows several advantages including the ease and low cost of fabrication, large-scale manufacturability, and controllable thickness. The major problem of filtered 3DSs is the restacking of 2D nanosheets once the film is dried. To address this issue and to preserve the porous structure after drying, several techniques have been developed including the surface charge control of 2D materials [137], the addition of non-volatile solvents [138] and spacing layers [139],

and post-filtration processing [140]. Through mediating the surface charge of MoS_2 nanosheets with pH values, the electrostatic repulsion between different layers prevents the restacking after filtering MoS_2 dispersions to form freestanding porous MoS_2 hydrogels [137]. Adding carbon nanotubes (CNTs) as spacing layers in the filtration process is also reported to be an effective way to maintain the scaffold structures of 3D MoS_2/rGO/CNTs [139]. Inspired by the seashell nacre, Hong group fabricated BN nanosheets (BNNSs)/gelatin nanocomposite via a vacuum filtration-induced self-assembly technique [Fig. 4D] [141]. The BNNSs were firstly decorated with hyperbranched polyglycerol (HPG). During the vacuum filtration process, electrostatic interactions between the functional groups on HPG and gelatin chains bridged the interlayers to form a classic brick-and-mortar structure like nacre. In contrast, pure 2D BN films without gelatin and HPG were typically brittle and not freestanding, which limits their applications [141]. Recently, a freestanding 3D microporous MXene film was produced by Gogotsi group, where 2D MXene flakes were filtrated and wrapped on PMMA spheres followed by thermal removal of the PMMA polymers at 450 °C [Fig. 4E] [142].

Dip-coating

Dip coating or drip-drying is a common and facile method to assemble 2D nanoarchitectures onto porous templates, such as polyurethane (PU) and melamine-formaldehyde (MF) sponges and nickel foams, through van der Waals or electrostatic interactions. The general process is as follows: cleaned 3D scaffolds are cut into suitable sizes and dipped into a suspension of 2D nanosheets in ethanol followed by vacuum drying at a mild temperature, i.e. below 80 °C to assemble a thin layer of 2D nanomaterials on the 3D surfaces of the porous templates. The thickness of the coated 2D nanoarchitectures can be controlled by repeating the "dipping-coating" process. The schematic of the dip-drying process is illustrated in Fig. 4F [143]. Recently, Fan group fabricated a MoS_2/C coated PU sponge by electrostatic forced-induced self-assembly [24]. Similarly, MoS_2/MF sponges [144], BN/MF sponges [145], MXene/nickel foams [146] and MXene/MF sponges [143] composites were obtained through the simple dip-drying method. The major limitation of this method could be the instable peeling-off of 2D nanosheets from 3D substrates resulting from the weak interaction.

Cross-linking

The gelation of 2D materials dispersions can be promoted by adding crosslinking molecules. The BNNSs/PVA fibers [22] and hydrogels [147] can be obtained through mixing the solution of BNNSs and PVA, in which the strong hydrogen bonding between the hydroxyl groups of PVA crosslinkers and the nitrogen groups on BN facilitates the gelation. In addition to the direct gelation between 2D materials and crosslinkers, some 2D materials like BN can be evenly dispersed or distributed within gels made of gelatin [21], glutaraldehyde [148] and divinyltetramethyldisiloxane-bis(benzocyclobutene) [149]. MXene nanosheets can be also mixed with hydrogels made of cross-linked PVA to directly fabricate MXene hydrogels [150]. Besides the organic molecules, GO can be also applied as crosslinkers to form a 3D network architecture as a scaffold of MoS_2 nanosheets [Fig. 4G] [151]. Here, the formation of cross-linked network structures is ascribed to the electrostatic interaction between negatively charged GO and positively charged hollow carbon spheres (HCS).

Properties of 3D superstructures

The grand applications of 3DSs rely on the exceptional properties governed by the synthesis approaches. Table 1 summarizes the main properties (*i.e.*, surface area, electrical and thermal conductivity, mechanical property) of various 3DSs. Since the CVD technique imparts 3D superstructures, especially 3D GF, with high quality, this section mainly discusses the properties of CVD grown 3D GF and how they are regulated by the fabrication methods, which could be applicable to other 3DSs.

Surface area

Three-dimensional graphene foams derived from various templates through CVD have demonstrated high surface areas [59,60,152,153]. Those made of Ni foams offer a surface area up to 850 $m^2 g^{-1}$, which can be modulated by tuning the number of layers deposited with different deposition time and flow rate [59]. However, the intrinsic large pores of diameter from 200 to 500 μm in between the Ni foam struts limit the surface area. Two ways have been reported to address this problem. First, the surface area can be enhanced by filling the pores with rGO aerogel (1.68X) [87], ramified graphitic microdendrites (3.4X) [19], CNTs (3.3X) [154], and sintered nickel powders (68X) [19]. Second, the employment of nanoporous substrates with reduced pore sizes also greatly improves the surface area. For example, GF with a pore size of 5–10 μm possesses a surface area of 980 $m^2 g^{-1}$ [155]. When the pore size is further reduced to the range of 100 nm to 2.0 μm, a surface area as high as 1320 $m^2 g^{-1}$ can be obtained [68,82,83]. 3D BN also exhibits a surface area with a similar magnitude of that of 3D GF. Owing to the ultralow mass density of aerogels, 3D BN and TMD aerogels usually deliver ultrahigh surface area ranging from few hundreds to one thousand meter squares per gram. The detailed data can be found in Table 1. Those high surface areas are pivotal for the applications of 3DSs in energy conversion and storage as well as oil absorption.

Electrical conductivity

The electrical conductivity of CVD grown 3D GF ranges from 2 to 55 $S cm^{-1}$ [59,60,156], which can be further enhanced by the following approaches. First, heteroatom doping can augment the charge carrier density, accordingly, improve the electrical conductivity. For example, after the N doping, the electrical conductivity of graphene foam can be increased from 2.86 $S cm^{-1}$ to 3.33 $S cm^{-1}$ [87]. Second, the low electrical conductivity is a result of the porous structure, which makes the electron-transfer pathway longer [72]. So the graphene pellets synthesized from compressed Ni powders reduces the pore size to 2 nm and results in the conductivity of 148 $S cm^{-1}$ [72]. It is worth noting that the intrinsic metallic conductivity of MXene endows 3D MXenes with outstanding electric conductivity as high as 200 $S cm^{-1}$ [142,157]. The high electrical conductivities of 3DSs promise the applications in energy conversion and storage, and sensing of mechanical and gaseous clues.

Thermal conductivity

The thermal conductivity of 3D GF depends on the CVD growth time and etchant used to remove the metallic template [158]. Changing the etchant from HCl to milder $Fe(NO_3)_3$, increased the thermal conductivity from 0.26 $W m^{-1} K^{-1}$ to 0.71 $W m^{-1} K^{-1}$ due to the improved integrality of graphene foam [158]. Longer growth time results in thicker graphene layer and thus, higher thermal conductivity (2.12 $W m^{-1} K^{-1}$ for 3-h growth; 0.71 $W m^{-1} K^{-1}$ for 1-h growth) [158]. Moreover, the air residing in the pores of GF could lead to a large convective thermal resistance between the air inside the pores to the surface of the graphitic struts. Li group sintered nickel powders on nickel foams to synthesize GF with reduced pore size, resulting in high thermal conductivity of 16.3 $W m^{-1} K^{-1}$ [76]. The same group also grew long continuous CNTs to form secondary

Table 1
Synthesis and properties of 3D superstructures made of 2D materials.

Materials	Methods	Surface Area ($m^2 g^{-1}$)	Pore Size (μm)	Mechanical Property	Conductivity		Ref.
					Electrical ($S cm^{-1}$)	Thermal ($W m^{-1} K^{-1}$)	
GF	CVD		ST: 6% (pristine GF)		\	\	[57]
GF	CVD	850	ST: 95% w/ PDMS		10	\	[59]
GF	CVD	392	~200–500	\	55	\	[60]
GF	CVD	\	~200–500	\	Electrical: 2 [156], 7.2 [208]		
GF	CVD	\	ST: 187% w/ PDMS		11.6	\	[232]
GF	CVD	\	590	\	\	1.7	[158]
GF	CVD		E: 1.2–1.5 MPa; hardness: 19.9–26.1 kPa		\	\	[160]
CNT/GF	CVD	\	250	\	\	19	[159]
GF/PDA/APTS/PDMS	CVD	E: 2.97 MPa; TS: 3.07 MPa; ST: 89.4%			\	28.77 (i.p.)	[211]
Compressed GF	CVD	\	\	\	\	82 (o.p.)	[98]
GF/PLC	CVD		E: 254 kPa; TS: 184 kPa; ST: 2763%		\	\	[25]
RPGF	CVD	$0.44 m^2 cm^{-3}$	~100	\	\	\	[19]
N-doped GF (NG)	CVD	786	259 nm	\	\	52	[83]
N, S-doped GF	CVD	1320	100–300	\	\	\	[82]
GF	CVD	980	5–10	\	\	\	[155]
GF	CVD	145	~1–5	\	17.5	\	[71]
N-doped GF	CVD	656	~10–40	\	\	\	[75]
GF	CVD	24.2	44–88	\	\	16.3	[76]
g-RACNT	CVD	526.91	~100 nm	\	\	\	[61]
N-doped rGO paper	Filtration	298	100 nm–10	\	316	\	[85]
GF-NG	Freeze-drying	583	~10–100	\	3.33	\	[87]
GO hybrid aerogels	3D Printing	212	~50	\	120	\	[123]
Graphene pellets	CVD	80	2 nm	\	148	\	[72]
BN foam	CVD	166	0.2–0.5	E: 13.2 MPa·$cm^3 g^{-1}$; MCS: 90%			[103]
Compressed BN foam	CVD	\	\	\	\	62 (o.p.)	[98]
BN foam	CVD	180	~80	\	\	\	[104]
hBNAGs	CVD	1080	\	\	\	0.0024	[102]
BNPMs	Thermolysis	1406	~5–40	\	\	\	[109]
BN foam	Cross-linking	\	~100	\	\	5.19 (i.p.);	[21]
BN foam	Thermolysis	773	1–100	\	\	0.035	[20]
BNNSs/PVA	Cross-linking	\	\	\	\	1.94 (o.p.)	[22]
BN aerogel	CVD	1051	12–21.5 nm	\	\	\	[101]
BNNS/gelatin	Filtration		E: 31.1 GPa; TS: 148.7 MPa		\	\	[141]
BN/PVA hydrogels	Freeze-drying	124.4	\	\	\	\	[133]
OH-BNNS/PVA	Cross-linking		E: 46 kPa; TS: 0.27 MPa; ST: 930%		\	0.6432	[147]
MoS_2/GA	Thermolysis	691	10–200 nm	\	1.12	\	[113]
WS_2@Ni foam	Hydrothermal	63.5	200–500	\	\	\	[130]
VO_2/g@NiS_2 aerogel	Hydrothermal	141.4	17.1 nm	\	\	\	[132]
WS_2 aerogel	Thermolysis	620	20–150 nm	\	\	\	[246]
MoS_2/rGO hydrogel	Freeze-drying	222.3	\	\	7.14	\	[134]
MXene porous film	Filtration	\	2–3	\	200	\	[142]
3D Ti_3C_2	Self-assembly	165.3	40–300 nm	\	120	\	[157]
$Ti_3C_2T_x$ MrGOA	Freeze-drying	\	5–20	\	~7.0	\	[136]
MXene hydrogel	Cross-linking	\	\	ST: 3400%	\	\	[150]

Graphene radially aligned CNT (g-RACNT); N-superdoped graphene network structure (GF–NG); hexagonal boron nitride aerogels (hBNAGs); BN-based porous monoliths (BNPMs); cellulose nanofibers (CNF); hydroxylated BNNS (OH-BNNS); graphene aerogel (GA); VO_2/graphene@NiS_2 aerogel (VO_2/g@NiS_2 aerogel); MXene/rGO hybrid aerogel (MrGOA); in-plane (i.p.); out-of-plane (o.p.); young's modulus (E); tensile strength (TS); stretchability (ST); maximum compression strain (MCS).

graphitic networks to fill in the interspace of GF, which further improved the conductivity to $19 W m^{-1} K^{-1}$ [159]. Besides, compressing the GF can remove the air inside the porous structure and thereby enhancing the thermal conductivity from $1.2 W m^{-1} K^{-1}$ to $86 W m^{-1} K^{-1}$ [98]. On the other hand, 3D BN superstructures exhibit thermal conductivities at a similar level of that of 3D GF. The high thermal conductivities enable both 3D GF and BN to be utilized for thermal energy dissipation.

Mechanical property

The elastic modulus of 3D GF is 1.2–1.5 MPa and the hardness is 19.9–26.1 kPa [160]. The high elastic modulus is attributed to the graphene branch alignment that allows the strut to sustain high load during in-plane tensile stretching. However, the low hardness results from branch bending and elastic depression of branch walls under the compression, which does not utilize the extraordinary mechanical property of 2D graphene. Incorporating polymers, such as PDMS and Ecoflex, with 3D GFs has been widely adopted to improve the stretchability [59], which is to be discussed in the section of mechanical sensing. In contrast, 3D BN architectures usually exhibit superelasticity [100,103]. For instance, cellular interconnected tubular BN network fabricated from CVD conversion method can sustain a maximum compressive strain of 90% and afford a density-normalized elastic modulus of ~13.2 MPa $cm^3 g^{-1}$ [103].

Applications of 3D superstructures

Energy conversion: fuel cells, solar cells, water splitting, and thermoacoustic sound generation

Energy conversion technologies including fuel cells, dye-sensitized solar cells (DSSCs), and water splitting devices leverage the unique properties 3DSs to optimize the efficiency and selectivity of catalytic reactions. Electrochemical catalysis involves chemical reactions that occur at catalytically active sites, and the performances of those devices can be improved by increasing the specific surface area of a catalytic material [161,162], the density of active sites [91], and/or by incorporating other active materials, e.g.

metals [163,164], metal oxides [161], and polymer catalysts [165]. Defect sites that are usually more catalytically active, have also been engineered via heteroatom doping [82] or post-synthesis plasma treatment [17]. Compared with single- or few-layer 2D materials, the unique features of 3D architectures make them more appealing for such applications. The non-agglomerated morphology and porous structure of 3D superstructures facilitate the loading and dispersion of catalysts. Moreover, the electrically interconnected graphitic or MXene scaffolds promote rapid electron transport between the reaction sites and the supporting electrode.

Fuel cells

Fuel cells that convert chemical energy from fuels, e.g., hydrogen, methanol, and ethanol, into electricity through electrochemical reactions with oxygen or other oxidizing agents hold great promise as future energy conversion devices. At the anode, a catalyst is normally employed to assist the oxidation of the fuels. At the cathode of fuel cells, the oxygen reduction reaction (ORR) is kinetically sluggish, dominating the full potential of fuel cells. 3D GF decorated with Pt NPs improved electrocatalytic activity towards both reactions in comparison with bare Pt NPs [Fig. 5(A, B)] [163,164]. The unique advantages of 3D structures in enhancing ORR catalysis are further confirmed in the 3D GFs loaded with valence transition metal oxides/sulfides such as mesoporous $NiCo_2O_4$ nanoplates [161] and $NiCo_2S_4$ nanosheets [162]. Without the incorporation of active materials, 3D GFs with boron and nitrogen doping also exhibited substantially augmented ORR electrocatalytic activities [17]. This is because doped B and N atoms act as active sites for ORR via charge transfer with neighboring C atoms and enhance the electroactive specific surface areas. Furthermore, the interaction between adjacent N and B atoms also reduces the size of the bandgap.

Dye-sensitized solar cells

Dye-sensitized solar cells (DSSCs), emerging as an economical alternative to silicon solar cells, consist of three components, *i.e.*, a dye-sensitized TiO_2 photoanode, an electrolyte solution with an iodide/triiodide redox couple, and a counter electrode (or cathode). Under solar irradiation, an electron-hole pair is created in the molecular dye in contact with the TiO_2 anode. The holes oxidize iodide to triiodide at the electrolyte interface; the electrons are injected into TiO_2 anode and travel through an external circuit to the cathode where triiodide is reduced back to iodide. The reduction of triiodide is usually facilitated by catalysts such as Pt. Porous 3D GF is a promising, inexpensive alternative to Pt [Fig. 5C] [107]. The DSSC's performance can be further improved by increasing the number of defective sites via assembling small-sized laser-reduced graphene quantum dots (L-GQDs) on 3D GF [153]. 3D GFs were also exploited as photoanodes to improve performances of DSSCs [166,167]. By mixing 3D GF with TiO_2 powder as photoanodes [Fig. 5D] [167], both the dye absorption and electron lifetime can be enhanced, which improves the power conversion efficiency.

Water splitting

Water splitting is an environmentally friendly technology that converts solar or electrical energy into hydrogen gas, a carbon-free fuel [168]. A water splitting device requires two electrodes: an anode and a cathode supported with their respective oxygen evolution reaction (OER) and hydrogen evolution reaction (HER) catalysts. The N, S co-doped GF grown at 500 °C was reported to exhibit high catalytic activity towards HER [Fig. 5E] [82]. The improved catalytic properties of NS500 can be attributed to defects caused by doping and low-temperature growth. The poor electrical transport and ineffective electrical contact to catalysts limit the manifestation of high catalytic activity of 2D TMDs towards water splitting. The 3D TMD hybridized with conductive materials are expected to exhibit enhanced performance for HER or OER due to their high surface area and rapid proton transfer during the catalytic process. Examples includes WS_2/GF [169], $MoS_{2(1-x)}Se_{2x}/NiSe_2$ foam [Fig. 5F] [105,106]. Some of the 3D TMD structures (Graphite/CoS_2 foam [170]) even can work as bifunctional catalysts for both HER and OER reactions. 3D conductive MXene networks have also been utilized as conductive scaffolds for water splitting. For instance, ultrafine CoP nanocrystallites anchored on 3D Ti_3C_2/MXene architectures were utilized as bifunctional electrodes for water splitting with enhanced activities [Fig. 5G] [157], which outperformed both CoP/non-3D-Ti_3C_2/MXene and CoP/3D-rGO.

Thermoacoustic devices

Owing to the excellent electrical and thermal conductivities, recently, graphene has been exploited in electrodes for thermoacoustic devices. The electrical current passing through the graphene generates heat (Joule heating), and the pores of the 3D structures allow heat transfer to the surrounding air, which generates oscillations and produces sound. Two factors control the efficiency of thermoacoustic devices, *i.e.* the heat capacities per unit area (HCPUA) of the electrode and the substrate [16]. Low HCPUA is desirable for improving the kinetics of heat transfer to the surrounding air. The applications of various nanomaterials including single- or few-layer graphene have been demonstrated in thermoacoustic devices owing to their low HCPUA [16]. A porous substrate provides even greater specific areas for heat exchange between electrodes and air. As a result, the 3D GF can readily offer enhanced performances compared to those of graphene films when integrated as thermoacoustic electrodes, as demonstrated by both Ren group [16] and Jung group [Fig. 5H] [171].

Energy storage: supercapacitors and rechargeable batteries

Supercapacitors

Supercapacitors that exhibit large power density, long cycling lifetime, and high charge/discharge speeds have the potential to meet the growing demand for energy storage. Based on the charge storage mechanism, supercapacitors can be categorized into electrical double layer capacitances (EDLCs) that store electrical energy via an electrostatic charging process via adsorption of ions at the interface between the active electrode and the electrolyte and pseudocapacitors that store electrical energy by rapid and reversible redox reactions at the interface of active materials. Hence, pseudocapacitors usually deliver much higher energy density than EDLCs. However, pseudocapacitive materials exhibit extremely low electric conductivities and have to be loaded onto conductive supports to fully manifest their high theoretical pseudocapacitances. Recently, substantial progress has been made on the use of 3DSs as either EDLC materials [61,172] or as conductive electrode supports of pseudocapacitors [18,19,60]. The porous structure of 3DSs not only facilitates the access of electrolytes to the entire surface of an electrode but also provides facile electron transfer pathways for the active nanomaterials, effectively enhancing the performances of both EDLCs and pseudocapacitors. The performance values of 3DSs based supercapacitors are summarized in Table 2.

The ultrahigh theoretical specific surface area (SSA) of a single graphene sheet ($2630\ m^2\ g^{-1}$) is appealing for the application of EDLCs. Various approaches have been developed to synthesize 3D GFs that consist of single or few-layer graphene sheets to manifest the high EDLCs [78,173]. Hybridizing 3D GF with various types of carbonaceous materials, such as CNTs [Fig. 6A] [61,172] and rGO [Fig. 6B] [87], can increase the SSA [172], alter the surface to be hydrophilic [87], which further improves the EDLC.

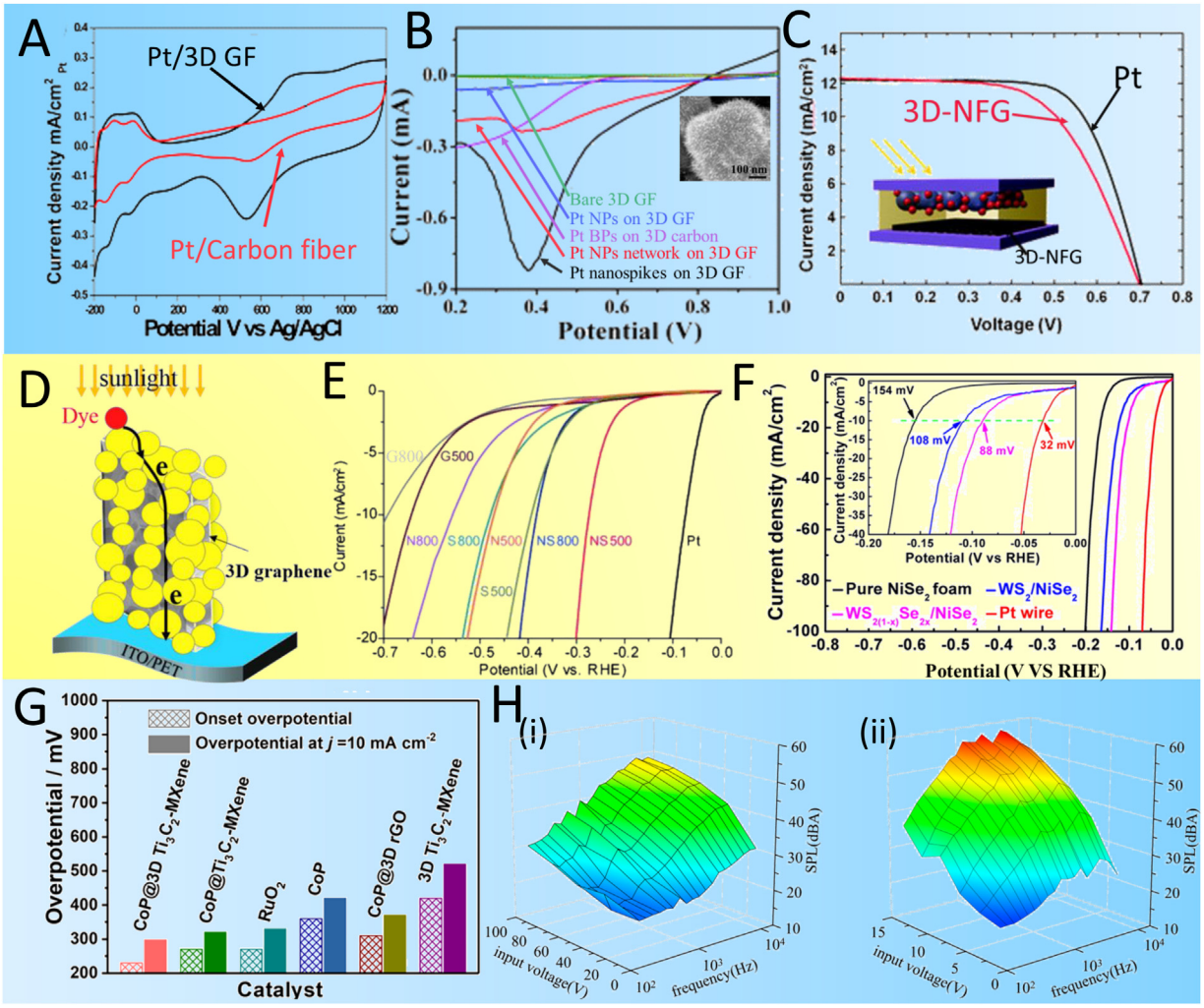

Fig. 5. Applications in energy conversion. (A) Cyclic voltammograms of Pt/3D-graphene and Pt/CF catalysts in H_2SO_4 [163]. (B) ORR polarization curves of Pt nanostructures with different morphologies on 3D GF; inset: SEM of Pt nanospikes [164]. (C) Photocurrent-voltage (I–V) curves for DSSCs with 3D-NFG CE and Pt CE [107]. (D) Schematic of the DSSC device and electron transport paths with 3D GF decorated with TiO_2 NPs network (in yellow) [167]. (E) HER polarization curves of the samples produced at different CVD temperatures and with different dopants compared to undoped nanoporous graphene [82]. (F) HER polarization curves of pure $NiSe_2$ foam, WS_2 on porous $NiSe_2$ foam, $WS_{2(1-x)}Se_{2x}$ on porous $NiSe_2$ foam and a Pt wire [106]. (G) A comparison of different MXenes catalysts in onset overpotential and $\eta j = 10\ mA\ cm^{-2}$ [157]. (H) The surface of the sound pressure level (SPL) as a function of the frequency and input voltage, (i) SPL of sound generated by the thermoacoustic device made of bilayer graphene on a polyimide film, (ii) SPL of sound generated by the thermoacoustic device made of three-dimensional 3-D graphene foam [171].
(A) Reproduced with permission from Ref. [163]. Copyright 2012, Royal Society of Chemistry. (B) Reproduced with permission from Ref. [164]. Copyright 2013, Royal Society of Chemistry. (C) Reproduced with permission from Ref. [107]. Copyright 2012, Royal Society of Chemistry. (D) Reproduced with permission from Ref. [167]. Copyright 2015, Elsevier. (E) Reproduced with permission from Ref. [82]. Copyright 2014, John Wiley and Sons. (F) Reproduced with permission from Ref. [106]. Copyright 2018, American Chemical Society. (G) Reproduced with permission from Ref. [157]. Copyright 2018, American Chemical Society. (H) Reproduced with permission from Ref. [171]. Copyright 2018, Elsevier.

Various pseudocapacitive materials can be decorated on 3D GF or its derivatives as pseudocapacitor electrodes, such as transitional metal oxides/hydroxides made of NiO [174], $Ni(OH)_2$ [66,175], Mn_xO_y [18,19,60], Co_3O_4 [176], and $Co(OH)_2$ [177], bimetal oxides/hydroxides [178,179]), metal chalcogenides [180,181], and conductive polymers [58,154,155,182]. These active materials can be deposited onto GF via hydrothermal synthesis, electrodeposition, and drop-casting. The enlarged surface area of 3D GFs largely boosts the active materials loading and contributes to ultrahigh specific capacitance. However, increasing the loading of pseudocapacitive materials on the conductive substrate impedes the ion transfer and migration process, which degrades the electrical conductivity and impairs the rate capability, coulombic efficiency, and cycling stability [60]. Several approaches have been developed to boost the mass loading without compromising the charge transfer and electrical conductivity, such as the incorporating conductive CNTs [Fig. 6C] [154] or polymers [Fig. 6D] [155], or increasing the surface area of GF via building secondary microstructures [Figs. 2B and 6 (E–G)] [18,19].

Besides 3D GFs, 3D TMDs and MXenes have also been explored in applications of supercapacitors because of the high theoretical capacitance of TMDs [183] and metallic conductive behaviors of MXenes [Fig. 6H] [146,184]. Similar to most pseudocapacitive materials, TMDs needs to be hybridized with conductive materials such as graphene [132], acetylene black coated Ni foams [129], polymers [Fig. 6I] [185] to fully manifest its pseudocapacitance.

Rechargeable batteries

Rechargeable batteries, particularly lithium-ion batteries, are of paramount importance for energy storage owing to their high energy density and working voltage, low maintenance (low self-discharge and no periodic discharge needed), and low toxicity. Three dimensional (3D) GFs have been widely applied as electrode supports in various rechargeable batteries, as either the anodes

Table 2
Performance of 3D superstructures based supercapacitors.

Materials	Loading ($mg\,cm^{-2}$)	Specific Capacitance[1]		C. E. (%)	Cyclability[2]	Ref.
		($F\,g^{-1}$)	($mF\,cm^{-2}$)			
nanomeshed graphene	\	255 @ 1 $A\,g^{-1}$	0.014	\	94.1 (2000)	[78]
graphene/MWCNT/Ni	\	286 $F\,g^{-1}$ @ 1.78 $mA\,cm^{-2}$ (Full)		\	99.34 (85,000)	[172]
g-RACNT	\		89.4	\	~100 (10,000)	[61]
GF-NG	1	380 @ 0.6 $A\,g^{-1}$	\	\	93.5 (4600)	[87]
GF/Ni-Co hydroxide	4	1900	7600	99	110 (15,000)	[178]
GF/MnO_2	0.1	465 @ 2 $mV\,s^{-1}$	\	93	81.2 (5000)	[60]
GF/CNT/MnO_2	0.6	215 @ 10 $mV\,s^{-1}$	130	95	90.2 (10,000)	[154]
GF/Co_3O_4/PEDOT/MnO_2	\	~ 400 @ 5 $A\,g^{-1}$ (Full)	\	\	90 (20,000)	[155]
MPGF/Mn_3O_4	0.15	538 @ 1 $mV\,s^{-1}$	\	\	90 (10,000)	[18]
RPGF/Mn_3O_4	3.91	164 @ 1 $mV\,s^{-1}$	820	98	88 (3000)	[19]
graphene pellets/MnO_2	79.6 wt%	395 @ 0.8 $A\,g^{-1}$	\	\	85 (5000)	[72]
GF/$NiCo_2S_4$	\	1454.6 @ 1.3 $A\,g^{-1}$	\	\	96 (3000)	[181]
GF/$Co(OH)_2$	0.21 mg	1636 @ 0.5 $A\,g^{-1}$	\	\	75 (1000)	[177]
GF/MoS_2	\	59 @ 1 $A\,g^{-1}$ (Full)	\	\	95 (2000)	[180]
NGF/CNT/MnO_2	70 wt%	284 @ 2 $mV\,s^{-1}$	3030	\	151.6 (15,000)	[247]
Ni/$MoSe_2$-acetylene black	\	2020 @ 1 $A\,g^{-1}$	\	\	107.5 (1000)	[129]
MoS_2/PANI/rGO aerogel	~4-5	618 @ 1 $A\,g^{-1}$	\	\	96 (2000)	[185]
VO_2/g@NiS_2 aerogel	\	1280 @ 1 $A\,g^{-1}$	\	\	86.2 (10,000)	[132]
Mn-SnS_2/graphene	\	523.51 @ 5 $mV\,s^{-1}$	\	\	98.57 (2000)	[248]
$Ti_3C_2T_x$ MXene/Ni foam	1.1 mg	499 @ 2 $mV\,s^{-1}$ (Full)	\	\	~100 (10,000)	[145]
$Ti_3C_2T_x$ MrGOA	\	34.6 m $F\,cm^{-2}$ @ 1 $mV\,s^{-1}$		~100	91 (15,000)	[184]
N-doped crumple GO	\	270 @ 1 $A\,g^{-1}$	\	\	97 (2000)	[117]

Coulombic efficiency (C. E.); polyaniline (PANI), multilevel porous graphite foam (MPGF).
[1] The specific capacitance is the half-cell value (three-electrode tests) based on the weight of active materials excluding the mass of electrode support (*i.e.*, GF, Ni foam, etc.). (Full): the full cell value (two-electrode tests).
[2] X (Y): (X) percentage capacitance is retained after (Y) cycles.

or cathodes of lithium-ion batteries (LIB) [14,186,187], lithium-sulfur batteries (LSB) [188,189], lithium-oxygen batteries [190], aluminum ion batteries (AIB) [191], and sodium-ion batteries (SIB) [192]. The porous conductive structures of 3D GFs provide large specific surface areas and high electrical conductivities, which not only facilitate the transport of electrons at the interface between an electrolyte and an electrode but also reduce fractures caused by the volume change of metals or metal oxide nanoparticles during charge/discharge cycles [8,193].

The decoration of 3D GFs with metal oxides, such as Fe_3O_4 [194], V_2O_5 [186], Co_3O_4 [195], MnO_2 [196], TiO_2 [73,89], $NiMoO_4$ [197], $ZnCo_2O_4$ [198]), lithium compounds [187,199], TMDs (MoS_2 [192], ReS_2 [112], FeS_2 [131]), Si NPs [200], CNTs [201,202], and conductive polymers [186] combines the respective advantages of active materials and GFs to assure improvement in capacity, rate capability and cycling life compared to those of simple 2D electrodes. The 3D GF based LIB electrodes have been well reviewed by several insightful articles [14,27]. Here, we highlight and summarize most recent work on LIB in Table 3. The electrodes of Li-S batteries usually suffer from extremely low loading (<2 $mg\,cm^{-2}$) and low weight content (<70 wt%) of sulfur, which can be addressed by a 3D hybrid graphene hierarchical network macrostructure comprising of electrically conductive CVD GF and rGO aerogel [Fig. 7A] [188].

Three-dimensional TMD based LIB anodes have attracted increasing attention in recent years due to their layered structures similar to that found in graphite while at a much larger interlayer spacing, which is favorable for rapid intercalation of Li^+ ions without notable volume change [126,131]. The capacity can be improved by facilitating the electron transfer with the hybridization of conductive graphene [Fig. 7B] [126] and CNTs [203] and by exposing the sulfur edge sites with the growth of vertical TMDs nanosheets [Fig. 7C] [112].

The high electrical conductivity, low Li-ion diffusion barrier, and high theoretical capacity of MXenes have been discovered both theoretically and experimentally and make these materials attractive for applications in rechargeable batteries [142,204,205]. Because of the abundant oxygen functional groups on the MXene sheets, Li nucleation can occur uniformly. High electrical conductivity and fast ionic-transport paths originating from a cross-linked network of MXene sheets enabled even Li growth. The interconnected voids in the aerogel can work as a stable host for high Li loading with mitigated volume fluctuation [Fig. 7D] [204].

Though the high specific surface of 3DSs benefits the ion transport in LIBs, it also exposes more redox sites that may cause an excess overpotential by increasing the interfacial resistance and pseudocapacitive side-reaction, impairing the energy efficiency, coulombic efficiency, and cycling stability [193,206]. The large porosity of 3DSs also results in low packaging density and thereby reduces the volumetric capacity [193]. Therefore, it is desirable to fabricate compact 3DSs with tunable interspaces and high volumetric performances. Recently, Fan group designed and fabricated an innovative ramified porous graphite foam (RPGF) with microdendrites filling the interspace between the graphite microstruts [Figs. 2B, 6 F] [19]. The microdendrites not only increase the surface by ~3X but also reduce the porosity from 81% to 63%, which is applicable to boost the volumetric energy storage [Fig. 6G] [19].

Energy dissipation: electromagnetic, thermal, and acoustic energies

Electromagnetic interference shielding

The widespread use of personal computers and portable electronics has generated severe electromagnetic interference (EMI) pollution. Great efforts have been devoted to developing EMI shielding materials. Electrically conductive polymer composites received intense attention owing to their lightweight, corrosion resistance, flexibility and low-cost compared to metal-based materials. The EMI shielding effectiveness (EMI SE) of polymer composites depends on the intrinsic conductivity, which can be improved by employing conductive fillers such as 3D GFs [156], MXenes [136], or conductive polymers, e.g. poly(3,4-ethylenedioxythiophene) polystyrene sulfonate (PEDOT: PSS) [Fig. 8A] [207]. The incorporation of CNTs on GFs [Fig. 8B] [208] can further boost the EMI SE by enhancing the dissipation of surface currents, expanding the conductive networks, and introducing numerous interfaces within the matrix.

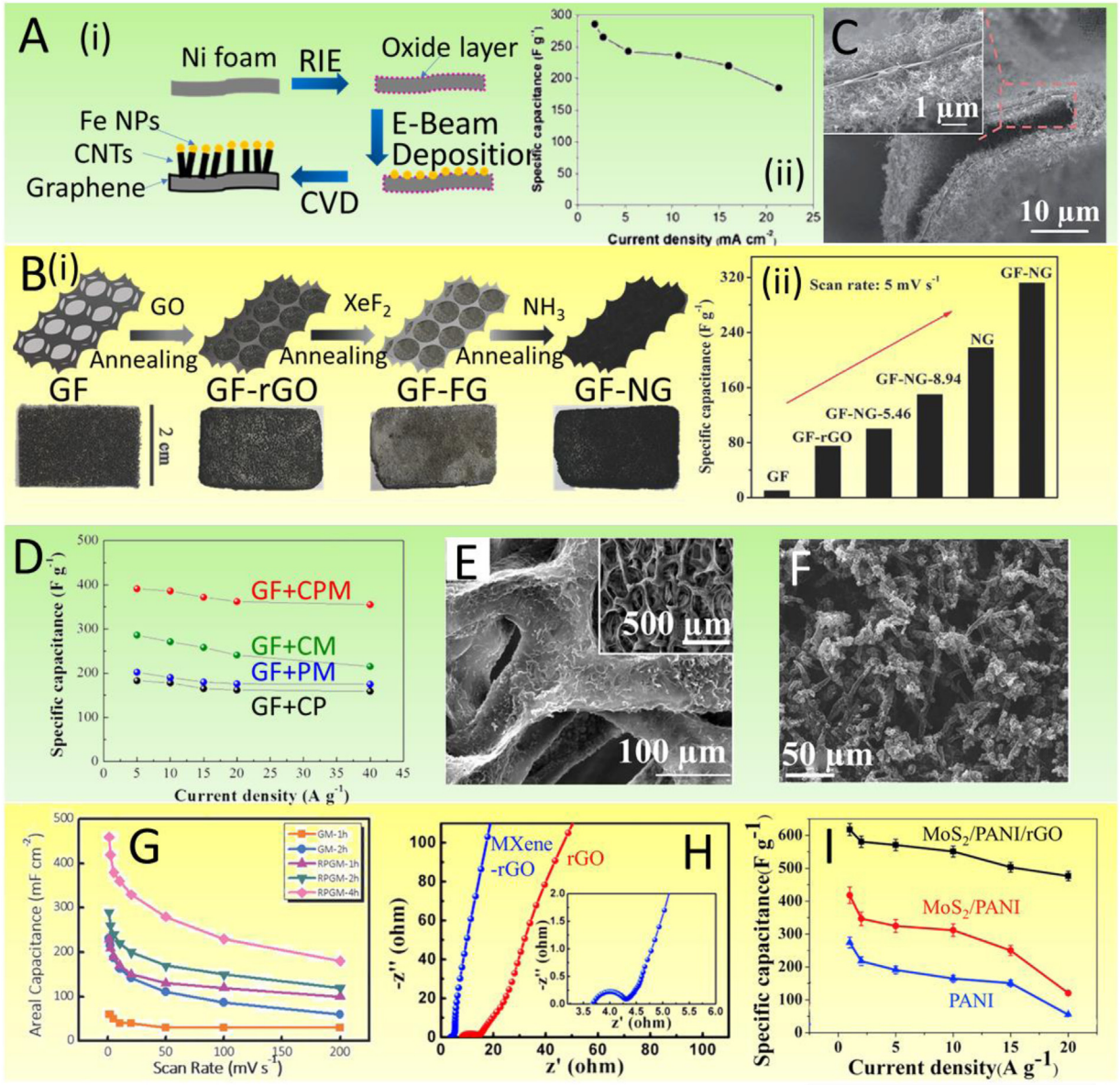

Fig. 6. Applications in supercapacitors. (A) (i) Schematic of the synthesis process of GF/MWCNT foams; (ii) specific capacitance values at different scan rates [172]. (B) N-superdoped 3D graphene networks (GF-NG) [87]: (i) fabrication process; (ii) specific capacitances of GF, GF-rGO, GF-NGs, and NG (nitrogen superdoped rGO) powder calculated by the CV curves at 5 mV s^{-1}. (C) Cross-sectional SEM images of GF/CNT branch [154]. (D) The specific capacitance of GF/Co_3O_4/PEDOT/MnO_2 at different current densities based on the mass of the whole weight of the electrode [155]. (E, F) SEM of (E) MPGFs [18] and (F) RPGFs [19]. (G) Specific capacitance comparison between RPGM (RPGF/Mn_3O_4) and GM (traditional graphite foams with Mn_3O_4) [19]. (H) MXene−rGO composite supercapacitors [184]: electrochemical impedance spectrum of pure rGO aerogel and MXene−rGO composite aerogel. (I) Degradation of specific capacitances in cycling tests of MoS_2/PANI/rGO aerogel supercapacitor [185].
(A) Reproduced with permission from Ref. [172]. Copyright 2013, Elsevier. (B) Reproduced with permission from Ref. [87]. Copyright 2017, John Wiley and Sons. (C) Reproduced with permission from Ref. [154]. Copyright 2014, Royal Society of Chemistry. (D) Reproduced with permission from Ref. [155]. Copyright 2014, American Chemical Society. (E) Reproduced with permission from Ref. [18]. Copyright 2017, John Wiley and Sons. (F, G) Reproduced with permission from Ref. [19]. Copyright 2018, John Wiley and Sons. (H) Reproduced with permission from Ref. [184]. Copyright 2018, American Chemical Society. (I) Reproduced with permission from Ref. [185]. Copyright 2016, Elsevier.

Thermal energy dissipation

The remarkable thermal conductivity of graphene and BN suggests their potential for heat management. The porous architectures of 3DSs provide enormous conductive pathways for electron and heat transfer, feasible for the application as heat sinks [20–22]. 3D BN is a highly effective thermal interfacial material (TIM) for heat sinks when infiltrated with PDMS/PVA, which can largely dissipate the thermal energy produced by LED chips [Fig. 8E] [22]. When loaded with phase change materials (PCMs), 3D GF can be applied as thermally conductive reservoirs for thermal energy storage [62, 209]. The thermal conductivity of the PCM can be improved through the incorporation of CNTs [Fig. 8C] [159] and hybrid graphene aerogel [210]. The functionalization of GF with polydopamine (PDA) and silane coupling agent (3-aminopropyltriethoxysilane, APTS) can increase the interfacial interaction between graphene and matrix, enhancing the in-plane thermal conductivity [Fig. 8D] [211].

Acoustic backing and sound absorbing

Graphene's superb thermal conductivity allows it to dissipate acoustic energy via the conversion of acoustic waves to thermal energy. When GF is embedded in polymers, the composite can be utilized as sound-absorbing materials (GF/PDMS) [212] or backing materials (GF/Epoxy filled with tungsten spheres) for acoustic attenuation [Fig. 8F] [213].

Table 3
Performance of 3D superstructures based rechargeable batteries.

Materials[1]	Loading (mg cm^{-2})	Specific Capacity[2]	C. E. (%)	Reversible Capacity[3]	Rate Performance[2]	Ref.
Ge-QD@NG	73.76 wt%	1220	76 (i.c.)	996 (200, 10 C)	801 (40 C)	[84]
$NiMoO_4$/GF	1	1088 (0.2)	85 (i.c.)	868 (150, 0.2)	770 (3.2)	[197]
$ZnCo_2O_4$/GF/Ni foam	\	2024*	55 (i.c.)	1223 (0.5, 240)	331 (4)	[198]
$NiCo_2S_4$/GF	\	2137*	75 (i.c.)	1295 (150, 0.5)	733 (3.2)	[162]
NG-MoS_2	\	1875 (0.1)*	63 (i.c.)	1205 (200, 0.1)	710 (5.0)	[126]
WS_2@SWCNT foam	0.6 ± 0.2	1050 (0.1)	63 (i.c.)	688 (1000, 1)	198 (5)	[203]
V-ReS_2/GF	77-87 wt%	539 (1)	\	200 (500, 1)	~100 (5)	[112]
SnS_2/CNT	45.82 wt%	1522 (0.1)*	90	502 (100, 0.1)	\	[249]
WS_2/CNT-rGO aerogel	\	749 (0.1)	53 (i.c.)	253(100, 0.2)	414 (5)	[250]
TiO_2(B)/EOGF	0.5	475 (0.05)	\	\	49 (40)	[89]
V_2O_5/PEDOT/GF	\	297 (1 C)	98 (i.c.)	\	115 (80 C)	[186]
FeS_2/GF	78.6 wt%	1244 (0.1)	88 (i.c.)	1080 (100, 0.2 C)	615.1 (5)	[131]
MoS_2/graphene aerogel	\	1220 (0.1)	\	\	375 (1)	[251]
MoS_2/GF	\	1400 (0.1)	75 (i.c.)	1127 (100, 0.25)	230 (4)	[192]
Ti_3C_2/rGO aerogel	70 wt%	149 (0.5 C)	\	\	63 (10)	[204]
MXene-rGO hybrid film	\	940*	\	212 (1000, 1)	98.9 (4)	[205]
Fe_3O_4/GF	\	\	99.9	1198 (400, 0.1)	250 (10)	[194]
Co_3O_4/GF	\	\	~100	986 (250, 0.1)	340 (2)	[195]
MnO_2/GF	\	\	\	1200 (300, 0.5)	>500 (5)	[196]
GF-rGO/S (LSB)	9.8, 83 wt%	1000 (0.2 C)*	\	645 (350, 0.2 C)	538 (2 C)	[188]
		The following four materials are electrodes of SIB				
$Ti_3C_2T_x$ porous film	\	390 (2.5 C)*	54 (i.c.)	295 (1000, 2.5 C)	120 (25 C)	
Mo_2CT_x porous film	\	400 (2.5 C)*	51(i.c.)	290 (1000, 2.5 C)	125 (25 C)	
V_2CT_x porous film	\	470 (2.5 C)*	55. (i.c.)	310 (1000, 2.5 C)	170 (25 C)	[142]
MoS_2/GF	\	\	67 (i.c.)	290 (50, 0.1)	\	[192]
plasma-etched GF (AIB)	\	148 (2)	98	~123 (10,000, 5)	123 (5)	[191]

Initial cycle (i.c.); Ge-quantum-dot/nitrogen-doped-graphene (Ge-QD@NG); edge-oriented multilayer graphene foam (EOGF); single-wall CNT (SWCNT); V-ReS_2 (vertical ReS_2).

[1] The materials are electrodes of LIB unless otherwise specified.
[2] X (Z): (X) capacity (mAh^{-1} g^{-1}) at Y current density (A g^{-1}).
[3] X (Y, Z): (X) capacity (mAh^{-1} g^{-1}) after (Y) cycles at Y current density (A g^{-1}).
* If the specific capacity is not provided, the value is the capacity at the initial discharging.

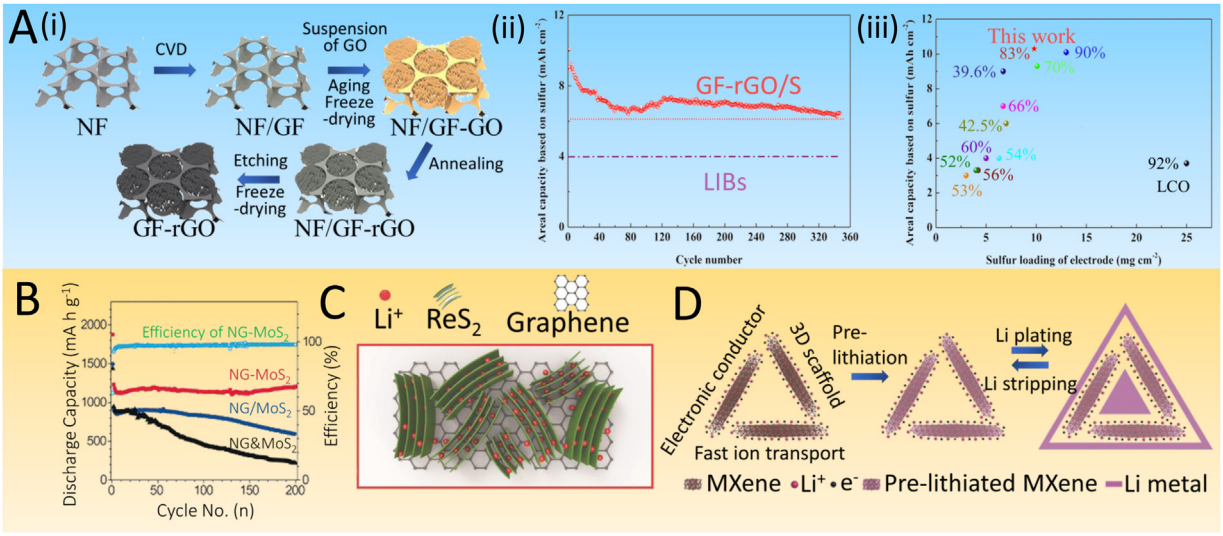

Fig. 7. Applications in rechargeable batteries. (A) 3D GF–rGO hybrid nested hierarchical network macrostructure [188]: (i) schematic of the fabrication procedure; (ii) comparison of areal capacity of the GF–rGO/S cathode with 9.8 mg cm^{-2} sulfur loading and 83 wt% sulfur content with LIB cathodes (purple dotted line); (iii) comparison of areal capacity and sulfur weight percentage of the GF–rGO/S cathode with recently reported Li–S cathodes with high sulfur loading. (B) Cycling performance at 0.1 A g^{-1} of the NG–MoS_2, NG/MoS_2, and NG&MoS_2 cathodes for lithium-ion batteries [125]. (C) V-ReS_2/3DGF [112]: schematic of lithium intercalation. (D) Schematic of the Ti_3C_2 MXene aerogel scaffolds for Li metal anodes [204].
(A) Reproduced with permission from Ref. [188]. Copyright 2015, John Wiley and Sons. (B) Reproduced with permission from Ref. [126]. Copyright 2016, John Wiley and Sons. (C) Reproduced with permission from Ref. [112]. Copyright 2018, John Wiley and Sons. (D) Reproduced with permission from Ref. [204]. Copyright 2018, John Wiley and Sons.

Sensing: electrochemical, optical, mechanical, and gaseous clues

Electrochemical sensing

Electrochemical sensors produce electrical current when the analyte molecules of interest participate in an electrochemical reaction at the surface of the sensor in the electrolyte. The sensitivity, detection limit, and linear range of detection are vital parameters in characterizing the performance of electrochemical sensors. Dopamine [214] and uric acid [77] can be directly oxidized electrochemically and are widely used in the evaluation of electrochemical sensors. As an electrode material, 3D GF is advantageous over the conventional glassy carbon due to the

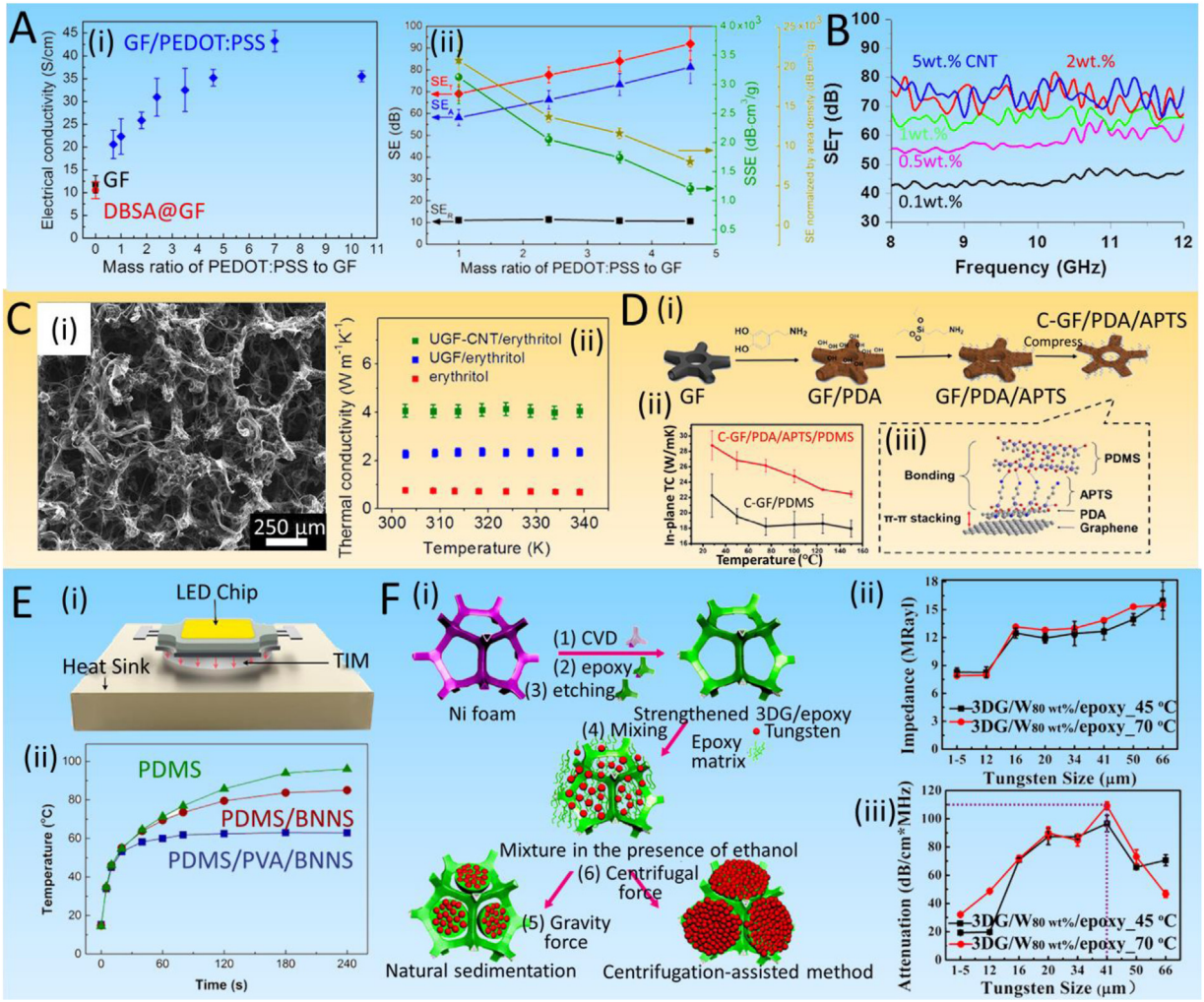

Fig. 8. Applications in energy dissipation. (A) GF/PEDOT:PSS composites [207]: (i) electrical conductivities versus the mass ratio of PEDOT:PSS to GFs with percent of connected pores in the inset; (ii) summary of SEs and specific SEs (SSEs) versus the mass ratio of PEDOT:PSS to GF. (B) EMI SE of GF/CNT/PDMS composites at 90.8% porosity with different CNT contents as a function of frequency [208]. (C) GF/CNT hybrid structure [159]: (i) SEM of CNTs/GF composites; (ii) thermal conductivities of different PCM (erythritol) composites. (D) GF/PDA/APTS/PDMS composites [211]: (i) illustration of fabrication procedures; (ii) in-plane thermal conductivities of GF/PDMS composites with and without the functionalization of PDA/APTS. (E) Performance of PVA/BNNSs for TIM [22]: (i) Schematic of the structure in an LED chip; (ii) the surface temperature variations of the LED chips against time. (F) 3D GF/W (3DG/W) composites [213]: (i) illustration of synthesizing process; (ii) comparison of acoustic impedance and (iii) acoustic attenuation of 3DG/W 80 wt %/epoxy composite films prepared by different methods as a function of W sphere sizes.
(A) Reproduced with permission from Ref. [207]. Copyright 2017, American Chemical Society. (B) Reproduced with permission from Ref. [208]. Copyright 2017, Elsevier. (C) Reproduced with permission from Ref. [159]. Copyright 2015, American Chemical Society. (D) Reproduced with permission from Ref. [211]. Copyright 2017, American Chemical Society. (E) Reproduced with permission from Ref. [22]. Copyright 2017, American Chemical Society. (F) Reproduced with permission from Ref. [213]. Copyright 2016, American Chemical Society.

enhanced surface area that allows more dopamine molecules to be collected for detection at a low concentration [214]. The detection limit can be further reduced through improving the surface area with the incorporation of CNTs [215], and the electrical conductivity via heteroatom doping [216]. However, many molecules such as H_2O_2 [217], glucose [218], and folic acid [219] can only be indirectly detected with the assistance of enzymes [215] or active materials such as catalytic metal particles (Pt [217], and PtRu [220]), electroactive metal oxides/hydroxides (MnO_2 [217], Mn_3O_4 [43], $Ni(OH)_2$ [221], and $Cu(OH)_2$ [218], ZnO [219]), and functional molecules [222]. Furthermore, redox reactions of metal oxides/hydroxides triggered by the presence of glucose are also utilized for nonenzymatic detection of glucose [218,221,223].

Optical sensing

Besides applications in electrochemical sensing, graphene has also been exploited as a surface-enhanced Raman spectroscopy (SERS) substrate for optical chemical detection [224,225]. Introducing three-dimensionality to the graphene/metal nanoparticles (NPs) hybrid structure would allow higher detection sensitivity of target analytes by utilizing the 3D focal volume [225]. Two plausible mechanisms have been proposed to account for SERS enhancement on graphene: (1) localized surface plasmon (LSP) resulted from the charge transfer from the graphene to NPs; (2) LSP confinement on graphene could focus the electromagnetic wave into a smaller area and shorter wavelength (λ), which further enhances the intensity of the reflected electromagnetic field and hence SERS signal. Srichan group employed Ag NPs coated 3D GFs as a sensitive SERS substrate for methylene blue (MB) detection [226]. The 3D structure is useful for SERS-based chemical sensing due to high specific surface area and enhanced optical scattering. As shown in Fig. 9A, the scattered light from a large number of Ag NPs located on multi-layer graphene sheets in GFs may be cumulatively integrated, leading to higher Raman enhancement factor.

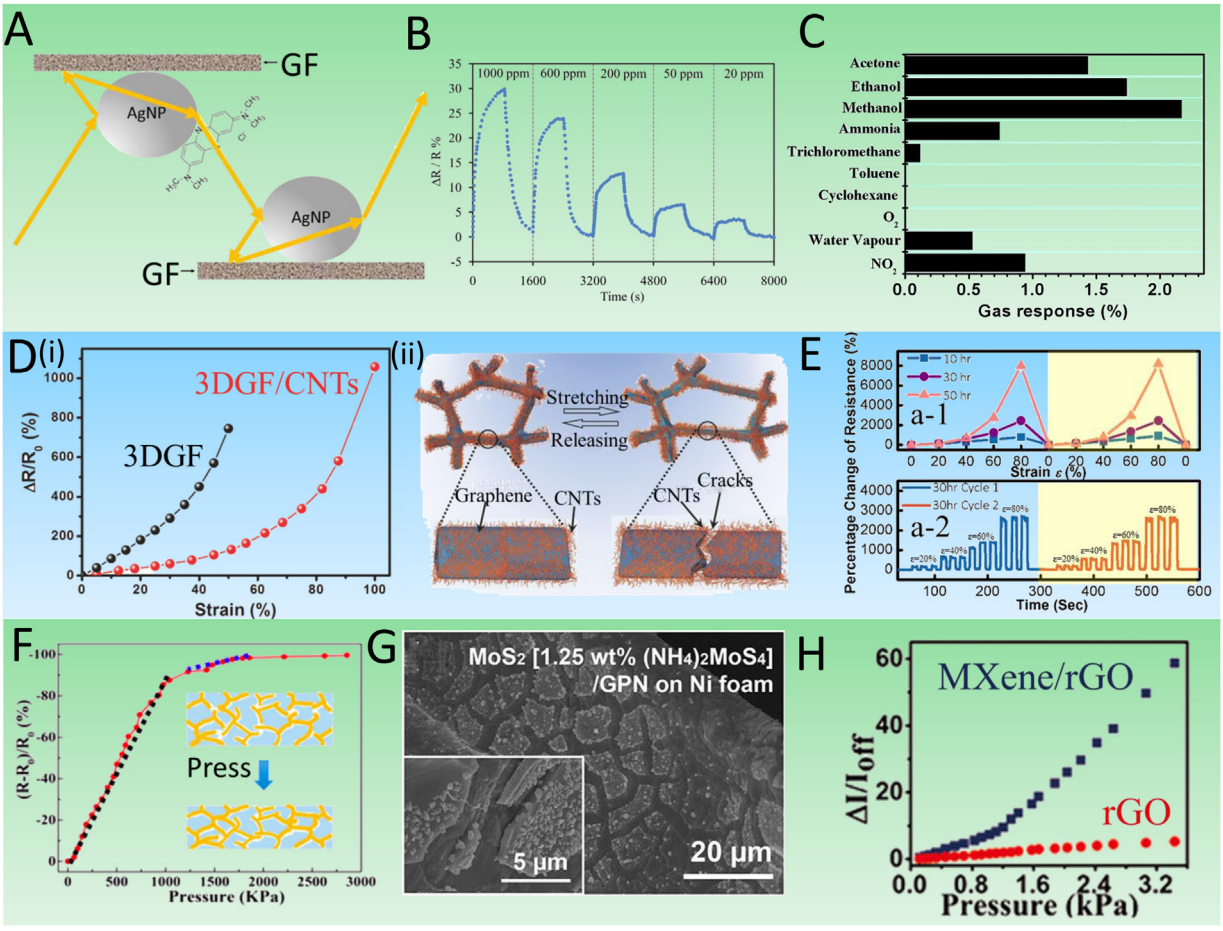

Fig. 9. Applications in sensing. (A) AgNPs/GF SERS [226]: multiple cascaded amplification scheme for a single molecule on AgNPs/graphene. (B) The sensitivity of the GF sensor for the detection of NH_3 [228]. (C) Maximal resistance changes upon exposure of 3D MXene framework to different gases [229]. (D) 3D GF/CNTs strain sensors [23]: (i) Electrical resistance response versus applied strains; (ii) schematic of the crack bridged by CNTs in 3D GF/CNTs. (E) Electrical resistance response versus applied strains of GF grown at different CVD time [230]. (F) Relative resistance variation of the 3D GF-PDMS composite with applied static compressive loading; inset: working mechanism responding to the applied pressure [233]. (G) MoS_2/GPN/Ecoflex pressure sensors [231]: SEM image. (H) Relative current change – compression strain curves of the MXene/rGO and rGO aerogel [135].

Gas sensing

Conductive 3D GFs [227,228] and MXenes [229] have demonstrated potential applications for gas sensing. The electrical conductivity of graphene and MXene can be readily changed upon the adsorption of gas molecules owing to charge transfer induced by the attached molecules that serve as electron donors or acceptors, such as NH_3, NO_2 [Fig. 9B] [228] and CO [227]. The surface terminations of oxygen, hydroxyl, and fluorine endow MXene with abundant active sites for gas absorption [229], exhibiting acute sensing of volatile organic compounds (VOC), e.g. methanol, ethanol, and acetone [Fig. 9C] [229].

Mechanical sensing: tensile-strain and pressure sensors

The high electric conductivity of 3D GF [59] and MXene [150] is sensitive to tensile and compressive strains, which allows them to be employed as a key element of piezoresistive strain sensors. Upon mechanical stretching or bending, the 3D interconnected networks start to deform, corresponding to a moderate resistance increase. At larger strains, microcracks on main struts generate and propagate, which effectively reduce the electron pathway and lead to a noticeable resistance increase. Pristine GFs can only sustain tensile strains of less than 6% [57]. The gauge factor (G), given by $G = (R - R_0)/(R_0\varepsilon)$, where R is the instant resistance at a strained state, R_0 is the initial resistance, and ε is the strain value, can be up to 1000. However, the low strain limit before the generations of cracks can restrict the detection of a large movement of human. The infiltration of GF with elastic polymers such as PDMS [59,230] and Ecoflex [231] can effectively improve the stretchability up to 95% [59]. The decoration of CNTs on GFs allows the strain to be distributed evenly under extremely deformed geometry CNTs and hence, largely enhances the strain tolerance [Fig. 9D] [23]. 3D GFs grown with long CVD time consist of ~60 layers graphene sheets, which provide a high density of lattice defects and result in an ultrahigh sensitivity [Fig. 9E] [230]. The reduction of the CVD temperature decreases the graphitization and thereby improves the gauge factor up to ~1500 [232].

3D superstructures of graphene and MXene also work as pressure sensors. When an external force compresses 3DSs, individual conductive branches start to attach locally and establish more electric conductive pathways, lowering the electric resistance [Fig. 9F] [232]. The decoration of cracked paddy-shaped MoS_2 on GFs further improves the sensitivity because of the generation of additional electric conduction pathways upon compression [Fig. 9G] [231].

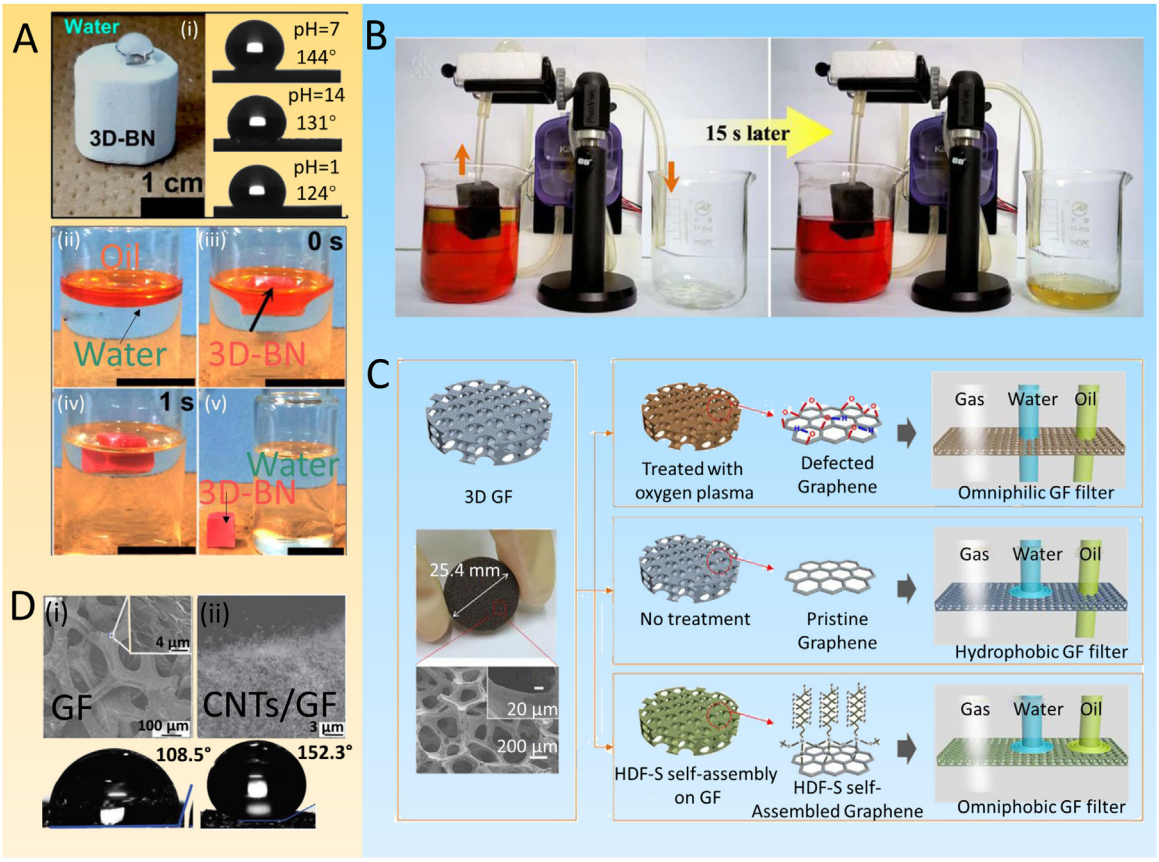

Fig. 10. Applications in oil/organic solvent absorption. (A) Wettability of 3D-BNF at different pH values of 1, 7, and 14; (i–v), photographs of hexane (dyed with a red agent) and its adsorption process by the 3D-BNF on the water surface. Scale bar: 2 cm [103]. (B) Continuous collection of gasoline in situ from a water surface with a MoS_2 coated MF sponge [235]. (C) Schematic of three diff ;erent types of GF by using surface treatment and their selective filtering properties [236]. (D) SEM and optical images of contact angle measurement of 3D GF (a) and 3D GF/CNTs (b) [234].
(A) Reproduced with permission from Ref. [103]. Copyright 2017, American Chemical Society. (B) Reproduced with permission from Ref. [235]. Copyright 2016, Springer Nature, is licensed under CC BY 4.0. (C) Reproduced with permission from Ref. [236]. Copyright 2015, Springer Nature, is licensed under CC BY 4.0. (D) Reproduced with permission from Ref. [234]. Copyright 2012, Royal Society of Chemistry.

The combination of the rGO's large specific surface area with the MXene's high electrical conductivity can also improve the performances of the composite pressure sensor compared to that of single-component rGO or MXene devices [Fig. 9H] [135]. The incorporation of MXenes in a hydrogel matrix made of PVA deliver both high tensile strain and compression sensitivities [150].

Environment remediation

Water decontamination: removing oil, dyes, and heavy metals

Three-dimensional (3D) architectures made of graphene, GO, BN, and TMDs have been developed for rapid removal of contaminants from water, including oil/organic solvents, heavy metal ions, and bacteria [12,15,27]. First, the high porosity of 3DSs provides large volume for the absorption of oil and other organic solvents. Second, the large delocalized π bond of graphene [63,234] and BN [Fig. 10A] [101,103] is favorable for interactions with oils and organic solvent via π-π bonding. Third, the covalent bonds between transitional metal and chalcogen atoms at the edge of the 2D TMD layers are strongly polarized, which could attract polar molecules and increase absorption capacity [Fig. 10B] [143,235]. Fourth, the wettability of the 3DSs can be tuned to realize either hydrophilicity or hydrophobicity and, thus, favor either the absorption of oil and organic solvents or soluble molecules from water [Fig. 10C] [236]. The CVD gown GF is hydrophobic with a contact angle of ~108.5°, which can be increased to 152.3° by incorporating CNTs [Fig. 10D] [234], or to 163° by coating with hydrophobic Teflon [237]. Finally, the formation of hydrogen bonds or complexation and electrostatic interactions enabled by the residual oxygenated functional groups on GO [15], activated materials loaded on BN [238], and chalcogen atoms on TMD [24] can be exploited to remove heavy metals ions such as Cd^{2+}, Pb^{2+}, Mg^{2+}, and Cu^{2+} and $Cr_2O_7^{2-}$ [15].

Solar steaming

Solar steaming is an emerging renewable and environment-friendly technique for water purification, which exploits solar energy to vaporize water at the air-liquid interface by efficient photothermal materials. Graphene exhibits broadband absorption of solar light, but its hydrophobicity hinders its application in solar steaming, which can be altered via N-doping [Fig. 11A] [83]. The wide-angle optical absorption is realized by the growth of vertical graphene nanoplates on 3D GF [Fig. 2F], thereby improving the solar-thermal energy conversion efficiency [Fig. 11B] [90]. Besides CVD grown GFs, the natively hydrophilic hydrogels and aerogels made of GO or partially reduced GO have also been developed for solar steaming [239], providing ultrahigh steaming rates [120,240]. The recent development of MoS_2/C coated PU sponges utilizes the effective photothermal property of carbon beads and high affinity between MoS_2 and heavy metal ions, contributing to the synergetic solar steaming and mercury removal as well as efficient bacterial removal [Fig. 11C] [24]. The same group further improved the solar-steaming efficiency and evaporation rate via exploring an origami strategy in making photothermal thin films into 3D roses [241]. A portable low-pressure water purification-collection uni-system is

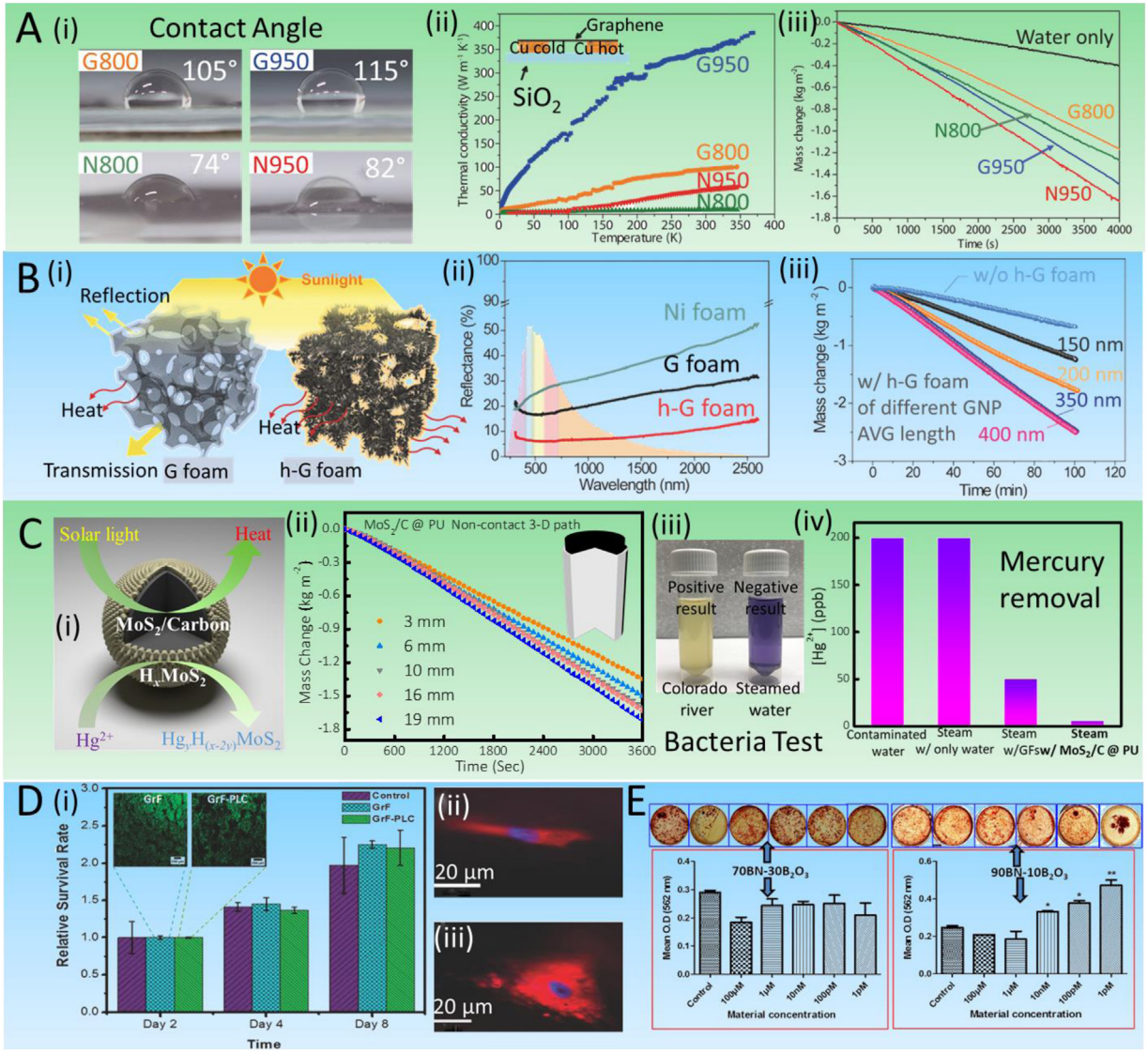

Fig. 11. Applications in solar steaming and tissue engineering. (A) N-doped nanoporous GFs [83]: contact angle measurements (i) and thermal conductivities (ii) of different porous graphene samples; (iii) evaporation mass loss of water with different porous graphene samples under 1 kW m^{-2} solar illumination. (B) Hierarchical graphene foams (h-G foam) [90]: (i) schematics of solar–thermal conversion difference between ordinary GF and h-G foam; (ii) diffuse reflectance spectra of different foam structures; (iii) water evaporation performance under standard solar irradiation (1 kW m^{-2}) with and without heat localization absorbers; the absorbers are h-G foam samples with different average length of vertical graphene nanosheets (150, 200, 350, and 400 nm). (C) MoS_2/C coated PU sponges [24]: (i) schematic of structure and functions of MoS_2/C microbeads; (ii) cumulative mass change of water versus time obtained from MoS_2/C @ PU sponges of different thickness; (ii) bacterial test of water from the Colorado River before and after solar steaming (yellow color: bacterial positive; purple color: bacterial negative); (iv) comparison of effectiveness of mercury removal by direct solar steaming, solar steaming assisted with GFs, and with MoS_2/C @ PU sponges. (D) GrF-PLC biocompatible scaffolds [25]: (i) Relative survival of hMSCs in GrF and GrF-PLC scaffolds in comparison to hMSCs grown in a monolayer within a cell culture flask; fluorescence microscopy images of stem cells on GrF (ii) and GrF-PLC scaffold (iii). (E) Calvarial osteoblast cells grown in osteoblast differentiation medium with a different amount of BNBO [243].
(A) Reproduced with permission from Ref. [83]. Copyright 2015, John Wiley and Sons. (B) Reproduced with permission from Ref. [90]. Copyright 2017, John Wiley and Sons. (C) Reproduced with permission from Ref. [24]. Copyright 2018, John Wiley and Sons. (D) Reproduced with permission from Ref. [25]. Copyright 2015, John Wiley and Sons. (E) Reproduced with permission from Ref. [243]. Copyright 2018, American Chemical Society.

also developed for enhancing the efficiency in water collection rate [241].

Cell culture scaffolds and tissue engineering

Tissue engineering, one of the most exciting areas in biomedical research, aims to generate living tissues *ex vivo* for *in vivo* replacement or therapeutic applications. The research has been carried out via material development, biochemical manipulation, cell culture, and genetic engineering. The biocompatibility of graphene [Fig. 11D] [25,242] and BN [Fig. 11E] [140,243] imparts capability for cell culturing. The porous structure of 3DSs, especially 3D GF, provides a microenvironment for the cells to grow within a 3-D biomimetic framework while simultaneously enhancing the functionality of the electroactive neural cells by providing highly conductive pathways for charge transport. Therefore, 3D GF and BN have been employed as biocompatible platforms for tissue engineering. The growth and differentiation of various cells, e.g., human mesenchymal stem cells (hMSCs) [25,242], myoblasts [244] and calvarial osteoblast cells [243] have been successfully demonstrated. Apart from pristine 3D GFs, Agarwal group developed a high-strength biocompatible scaffold by dip-coating biodegradable poly(lactic acid–poly-ε-caprolactone) copolymer (PLC) onto 3D GF (denoted as GrF-PLC) and enhanced the mechanical strength by

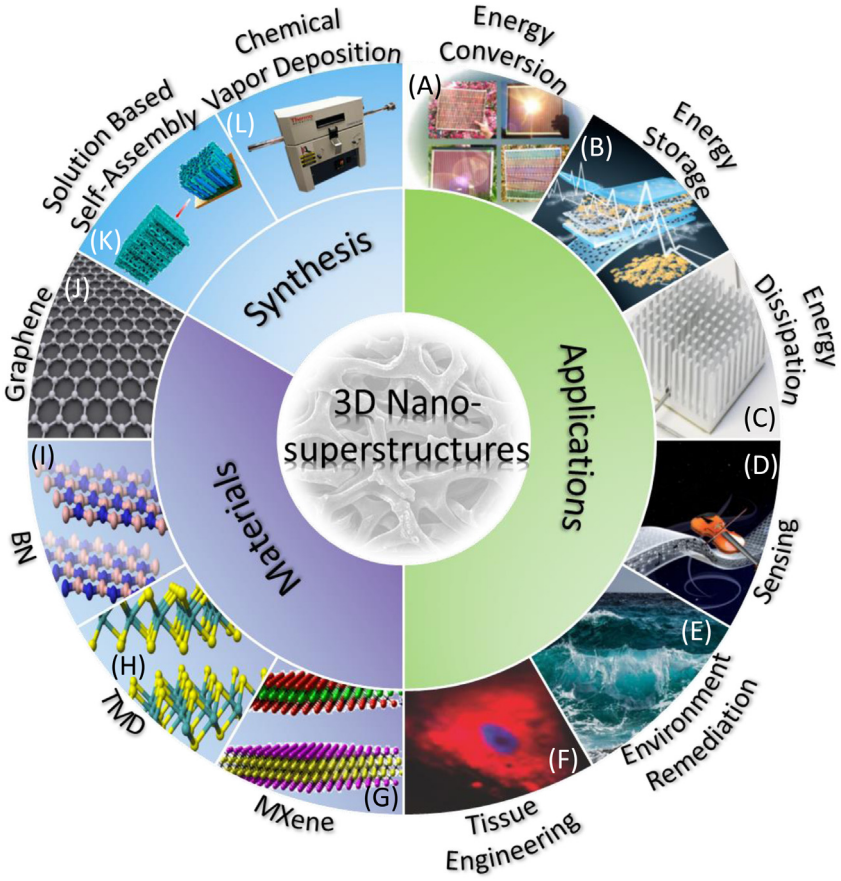

Fig. 12. Graphical summary of materials, synthesis methods, and applications of the 3DSs made of several 2D materials.
(A, C, H, I) Copyright has been released into the public domain by their authors. (B) Reproduced with permission from Ref. [18]. Copyright 2017, John Wiley and Sons. (D) Reproduced with permission from Ref. [23]. Copyright 2017, John Wiley and Sons. (E) Copyright, Pixabay License. (F) Reproduced with permission from Ref. [25]. Copyright 2015, John Wiley and Sons. (G) Reproduced with permission from Ref. [53]. Copyright 2015, American Chemical Society. (J) Copyright is licensed under CC BY-SA 3.0. (K) Reproduced with permission from Ref. [136]. Copyright 2018, American Chemical Society.

3100% and the ductility by 3700% [Fig. 11D-(i)] [25]. It was found that the higher strength of the GrF-PLC scaffold enabled the hMSCs to grow normally without undergoing large deformations [Fig. 11D-(iii)]; in contrast, the pristine graphene foam did not have sufficient strength to withstand cell-induced strains, resulting in the growth of hMSCs in a highly elongated morphology [Fig. 11D-(ii)] [25].

Outlook: potentials, challenges, and opportunities

In summary, we have portrayed a comprehensive list of 3DSs made of 2D materials with focuses on CVD grown graphene, h-BN, TMDs, and MXene. The general structure, unique characteristics, synthetic methods, and diverse applications of those 3DSs are thoroughly discussed. A graphical summary of materials, synthesis, and applications of 3D nanosuperstructures is exhibited in Fig. 12. In order to fully leverage their unique properties in a macroscopic device or composite, researchers and engineers must arrange 2D materials into 3D architectures that prevent aggregation and restacking. Great progress has been made in fabricating such 3DSs via high-temperature and vapor involved CVD synthesis (including thermolysis) and solution-based self-assembly. The detailed fabrication approaches vary for each category of 2D materials. For instance, 3D graphene, BN and TMD superstructures can be obtained through both methods, but 3D MXene can be only achieved by solution-based synthesis techniques. CVD growth highly depends on the employed templates that determine the size and distribution of pores, and gas precursors that govern the chemistry and lattice structures of obtained materials. As shown by the review of CVD-based GFs, the high-temperature of CVD reactions endows 3D superstructures with better crystallinity, electrical and thermal properties than those obtained from self-assembly. However, it remains a challenging task to sculpt the templates into desired features and sizes by design. This represents a great opportunity in future research, e.g. the combination of top-down fabrication leveraging 3D and bottom-up synthesis for structural realization. On the other hand, the solution-based synthetic approaches—hydrothermal reaction, dip coating, electrospinning, filtration, and freeze-drying—enable the fabrication of 3D superstructures—foams, films, hydrogel, aerogels—that are not limited by template availability or stability. Furthermore, the low temperature and liquid phase synthesis conditions make superstructures produced via template-free methods more amenable to functionalization and hybridization with other 2D materials or active nanomaterials. This advantage has been demonstrated in the synthesis of 3D BN, TMDs, and MXenes. However, the solution-based synthesis shares the same challenge in creating layers and features of 3DSs by rationality and design.

The great research interest of 3DSs made of 2D materials also lies in their broad promising applications, ranging from energy conversion/storage/dissipation, environment remediation, electrochemical/optical/mechanical sensing, to biomedical engineering. However, there are still a few challenges to be overcome before successfully commercializing those attractive materials. First, the lab-scale synthesis of 3D superstructures needs to be scaled up for mass production to meet the demand for industrial applications. The associated manufacturing issues should be addressed, e.g. to

obtain highly controllability of physical and chemical properties on a large scale and to achieve these goals with low cost. Precision and automated equipment for fabrication and in-situ testing should be investigated. Second, though 3D GF exhibits great potential in various aspects, its fragility makes it hard to be handled and transferred. Therefore, a study of improving the mechanical property of 3DSs with minimal additives needs to be continued. Third, most 3D composites have applications in technologies, e.g. energy storage devices and sensors, which must be integrated with external electronics or power supply to function as a complete device. However, up to now, very few reports covered the packaging and integration of 3D composites with other functional parts for practical uses. Comprehensive evaluations and resolutions of problems on the different material-, device-, system-level are desired. Fourth, the real application and excellent performance of 3D materials rely on the incorporation of many other active materials such as metal, metal oxides, polymers and other kinds of 2D materials. For instance, heterojunctions of distinct materials have been widely studied in the 2D material system for enhanced electronic and electrochemical performances [245]. There is a compelling interest of a rational integration of bespoke materials into 3D in order to further excavate new properties or boost performances for the desired application. Finally, up to now, only graphene and BN can be built as 3DSs without any foreign supporting substrates. It remains a daunting challenge but also an attractive research direction to create completely free-standing 3D TMDs and MXenes to copiously display unique characteristics of 2D materials.

Acknowledgments

This work is supported by National Science Foundation (Grant No. CMMI 1563382) and Welch Foundation (Grant No. F-1734).

References

[1] K.S. Novoselov, A.K. Geim, S.V. Morozov, D. Jiang, Y. Zhang, S.V. Dubonos, I.V. Grigorieva, A.A. Firsov, Science 306 (2004) 666–669.
[2] K.S. Novoselov, V.I. Fal'ko, L. Colombo, P.R. Gellert, M.G. Schwab, K. Kim, Nature 490 (2012) 192–200.
[3] J. Yin, J. Li, Y. Hang, J. Yu, G. Tai, X. Li, Z. Zhang, W. Guo, Small 12 (2016) 2942–2968.
[4] J. Zhu, P. Xiao, H. Li, S.A. Carabineiro, ACS Appl. Mater. Interfaces 6 (2014) 16449–16465.
[5] D. Voiry, J. Yang, M. Chhowalla, Adv. Mater. 28 (2016) 6197–6206.
[6] J. Pang, R.G. Mendes, A. Bachmatiuk, L. Zhao, H.Q. Ta, T. Gemming, H. Liu, Z. Liu, M.H. Rummeli, Chem. Soc. Rev. 48 (2019) 72–133.
[7] Y. Yi, X.-F. Yu, W. Zhou, J. Wang, P.K. Chu, Mater. Sci. Eng. R Rep. 120 (2017) 1–33.
[8] K. Shehzad, Y. Xu, C. Gao, X. Duan, Chem. Soc. Rev. 45 (2016) 5541–5588.
[9] J.-E. Kim, J.-H. Oh, M. Kotal, N. Koratkar, I.-K. Oh, Nano Today 14 (2017) 100–123.
[10] H. Jiang, P.S. Lee, C. Li, Energy Environ. Sci. 6 (2013) 41–53.
[11] V. Chabot, D. Higgins, A. Yu, X. Xiao, Z. Chen, J. Zhang, Energy Environ. Sci. 7 (2014) 1564–1596.
[12] Y. Shen, Q. Fang, B. Chen, Environ. Sci. Technol. 49 (2015) 67–84.
[13] S. Mao, G. Lu, J. Chen, Nanoscale 7 (2015) 6924–6943.
[14] S. Jin, Y. Jiang, H. Ji, Y. Yu,Adv. Mater. 30 (2018), 1802014.
[15] N. Yousefi, X. Lu, M. Elimelech, N. Tufenkji, Nat. Nanotechnol. 14 (2019) 107–119.
[16] Z. Zhang, H. Tian, P. Lv, Y. Yang, Q. Yang, S. Yang, G. Wang, T. Ren,Appl. Phys. Lett. 110 (2017), 093110.
[17] Y. Xue, D. Yu, L. Dai, R. Wang, D. Li, A. Roy, F. Lu, H. Chen, Y. Liu, J. Qu, Phys. Chem. Chem. Phys. 15 (2013) 12220–12226.
[18] W. Li, X. Xu, C. Liu, M.C. Tekell, J. Ning, J. Guo, J. Zhang, D. Fan,Adv. Funct. Mater. 27 (2017), 1702738.
[19] W. Li, M.C. Tekell, C. Liu, J.A. Hethcock, D. Fan,Adv. Funct. Mater. 28 (2018), 1800601.
[20] J. Lin, X. Yuan, G. Li, Y. Huang, W. Wang, X. He, C. Yu, Y. Fang, Z. Liu, C. Tang, ACS Appl. Mater. Interfaces 9 (2017) 44732–44739.
[21] Z. Tian, J. Sun, S. Wang, X. Zeng, S. Zhou, S. Bai, N. Zhao, C.-P. Wong, J. Mater. Chem. A 6 (2018) 17540–17547.
[22] J. Chen, X. Huang, B. Sun, Y. Wang, Y. Zhu, P. Jiang, ACS Appl. Mater. Interfaces 9 (2017) 30909–30917.
[23] Y. Cai, J. Shen, Z. Dai, X. Zang, Q. Dong, G. Guan, L.J. Li, W. Huang, X. Dong,Adv. Mater. 29 (2017), 1606411.
[24] W. Li, M.C. Tekell, Y. Huang, K. Bertelsmann, M. Lau, D. Fan,Adv. Energy Mater. 8 (2018), 1802108.
[25] A. Nieto, R. Dua, C. Zhang, B. Boesl, S. Ramaswamy, A. Agarwal, Adv. Funct. Mater. 25 (2015) 3916–3924.
[26] Y. Wu, J. Zhu, L. Huang, Carbon 143 (2019) 610–640.
[27] B.Y.Z. Hiew, L.Y. Lee, X.J. Lee, S. Thangalazhy-Gopakumar, S. Gan, S.S. Lim, G.-T. Pan, T.C.-K. Yang, W.S. Chiu, P.S. Khiew, Process Saf. Environ. 116 (2018) 262–286.
[28] X.H. Xia, D.L. Chao, Y.Q. Zhang, Z.X. Shen, H.J. Fan, Nano Today 9 (2014) 785–807.
[29] H.-F. Wang, C. Tang, Q. Zhang, Nano Today 25 (2019) 27–37.
[30] S. Jiang, S. Agarwal, A. Greiner, Angew. Chem. Int. Ed. 56 (2017) 15520–15538.
[31] J. Mao, J. Iocozzia, J. Huang, K. Meng, Y. Lai, Z. Lin, Energy Environ. Sci. 11 (2018) 772–799.
[32] S. Priyadarsini, S. Mohanty, S. Mukherjee, S. Basu, M. Mishra, J. Nanostruct. Chem. 8 (2018) 123–137.
[33] A.S. Mayorov, R.V. Gorbachev, S.V. Morozov, L. Britnell, R. Jalil, L.A. Ponomarenko, P. Blake, K.S. Novoselov, K. Watanabe, T. Taniguchi, A.K. Geim, Nano Lett. 11 (2011) 2396–2399.
[34] A.A. Balandin, Nat. Mater. 10 (2011) 569–581.
[35] C. Lee, X. Wei, J.W. Kysar, J. Hone, Science 321 (2008) 385–388.
[36] F. Bonaccorso, L. Colombo, G. Yu, M. Stoller, V. Tozzini, A.C. Ferrari, R.S. Ruoff, V. Pellegrini,Science 347 (2015), 1246501.
[37] R.R. Nair, P. Blake, A.N. Grigorenko, K.S. Novoselov, T.J. Booth, T. Stauber, N.M.R. Peres, A.K. Geim, Science 320 (2008) 1308.
[38] K.S. Novoselov, D. Jiang, F. Schedin, T.J. Booth, V.V. Khotkevich, S.V. Morozov, A.K. Geim, Proc. Natl. Acad. Sci. U. S. A. 102 (2005) 10451–10453.
[39] D.C. Marcano, D.V. Kosynkin, J.M. Berlin, A. Sinitskii, Z. Sun, A. Slesarev, L.B. Alemany, W. Lu, J.M. Tour, ACS Nano 4 (2010) 4806–4814.
[40] K.S. Kim, Y. Zhao, H. Jang, S.Y. Lee, J.M. Kim, K.S. Kim, J.H. Ahn, P. Kim, J.Y. Choi, B.H. Hong, Nature 457 (2009) 706–710.
[41] A. Reina, X. Jia, J. Ho, D. Nezich, H. Son, V. Bulovic, M.S. Dresselhaus, J. Kong, Nano Lett. 9 (2009) 30–35.
[42] X. Li, W. Cai, J. An, S. Kim, J. Nah, D. Yang, R. Piner, A. Velamakanni, I. Jung, E. Tutuc, S.K. Banerjee, L. Colombo, R.S. Ruoff, Science 324 (2009) 1312–1314.
[43] A. Bianco, H.-M. Cheng, T. Enoki, Y. Gogotsi, R.H. Hurt, N. Koratkar, T. Kyotani, M. Monthioux, C.R. Park, J.M.D. Tascon, J. Zhang, Carbon 65 (2013) 1–6.
[44] Y. Zhu, S. Murali, W. Cai, X. Li, J.W. Suk, J.R. Potts, R.S. Ruoff, Adv. Mater. 22 (2010) 3906–3924.
[45] A. Pakdel, Y. Bando, D. Golberg, Chem. Soc. Rev. 43 (2014) 934–959.
[46] Y. Lin, J.W. Connell, Nanoscale 4 (2012) 6908–6939.
[47] A. Falin, Q. Cai, E.J. Santos, D. Scullion, D. Qian, R. Zhang, Z. Yang, S. Huang, K. Watanabe, T. Taniguchi, Nat. Commun. 8 (2017) 15815.
[48] T. Ouyang, Y. Chen, Y. Xie, K. Yang, Z. Bao, J. Zhong,Nanotechnology 21 (2010), 245701.
[49] L.H. Li, J. Cervenka, K. Watanabe, T. Taniguchi, Y. Chen, ACS Nano 8 (2014) 1457–1462.
[50] R.J. Toh, Z. Sofer, J. Luxa, D. Sedmidubský, M. Pumera, ChemComm 53 (2017) 3054–3057.
[51] M. Chhowalla, H.S. Shin, G. Eda, L.-J. Li, K.P. Loh, H. Zhang, Nat. Chem. 5 (2013) 263–275.
[52] K.F. Mak, C. Lee, J. Hone, J. Shan, T.F. Heinz,Phys. Rev. Lett. 105 (2010), 136805.
[53] B. Anasori, Y. Xie, M. Beidaghi, J. Lu, B.C. Hosler, L. Hultman, P.R.C. Kent, Y. Gogotsi, M.W. Barsoum, ACS Nano 9 (2015) 9507–9516.
[54] C. Zhang, B. Anasori, A. Seral-Ascaso, S.-H. Park, N. McEvoy, A. Shmeliov, G.S. Duesberg, J.N. Coleman, Y. Gogotsi, V. Nicolosi,Adv. Mater. 29 (2017), 1702678.
[55] D. Er, J. Li, M. Naguib, Y. Gogotsi, V.B. Shenoy, ACS Appl. Mater. Interfaces 6 (2014) 11173–11179.
[56] L. Bai, H. Yin, L. Wu, X. Zhang, Comput. Mater. Sci. 143 (2018) 225–231.
[57] Y. Wang, L. Wang, T. Yang, X. Li, X. Zang, M. Zhu, K. Wang, D. Wu, H. Zhu, Adv. Funct. Mater. 24 (2014) 4666–4670.
[58] X. Zang, M. Zhu, X. Li, X. Li, Z. Zhen, J. Lao, K. Wang, F. Kang, B. Wei, H. Zhu, Nano Energy 15 (2015) 83–91.
[59] Z. Chen, W. Ren, L. Gao, B. Liu, S. Pei, H.M. Cheng, Nat. Mater. 10 (2011) 424–428.
[60] Y. He, W. Chen, X. Li, Z. Zhang, J. Fu, C. Zhao, E. Xie, ACS Nano 7 (2013) 174–182.
[61] Y. Xue, Y. Ding, J. Niu, Z. Xia, A. Roy, H. Chen, J. Qu, Z.L. Wang, L. Dai,Sci. Adv. 1 (2015), e1400198.
[62] M. Zhou, T. Lin, F. Huang, Y. Zhong, Z. Wang, Y. Tang, H. Bi, D. Wan, J. Lin, Adv. Funct. Mater. 23 (2013) 2263–2269.
[63] L. Shi, K. Chen, R. Du, A. Bachmatiuk, M.H. Rummeli, K. Xie, Y. Huang, Y. Zhang, Z. Liu, J. Am. Chem. Soc. 138 (2016) 6360–6363.
[64] X. Li, W. Cai, L. Colombo, R.S. Ruoff, Nano Lett. 9 (2009) 4268–4272.
[65] Q. Yu, J. Lian, S. Siriponglert, H. Li, Y.P. Chen, S.-S. Pei,Appl. Phys. Lett. 93 (2008), 113103.
[66] J. Ning, X. Xu, C. Liu, D.L. Fan, J. Mater. Chem. A 2 (2014) 15768–15773.
[67] J. Guo, A. Chan, W. Li, D.L. Fan, Chem. Mater. 29 (2017) 4991–4998.
[68] Y. Ito, Y. Tanabe, H.J. Qiu, K. Sugawara, S. Heguri, N.H. Tu, K.K. Huynh, T. Fujita, T. Takahashi, K. Tanigaki, M. Chen, Angew. Chem. Int. Ed. 53 (2014) 4822–4826.
[69] X.H. Xia, J.P. Tu, Y.Q. Zhang, Y.J. Mai, X.L. Wang, C.D. Gu, X.B. Zhao, J. Phys. Chem. C 115 (2011) 22662–22668.

[70] W. Jiang, H. Xin, W. Li, Mater. Lett. 162 (2016) 105–109.
[71] B.H. Min, D.W. Kim, K.H. Kim, H.O. Choi, S.W. Jang, H.-T. Jung, Carbon 80 (2014) 446–452.
[72] L. Zhang, D. DeArmond, N.T. Alvarez, D. Zhao, T. Wang, G. Hou, R. Malik, W.R. Heineman, V. Shanov, J. Mater. Chem. A 4 (2016) 1876–1886.
[73] S. Wang, G. Wang, X. Zhang, Y. Tang, J. Wu, X. Xiang, X. Zu, Q. Yu, Carbon 120 (2017) 103–110.
[74] T.M. Paronyan, A.K. Thapa, A. Sherehiy, J.B. Jasinski, J.S. Jangam, Sci. Rep. 7 (2017) 39944.
[75] Y. Wang, J. Huang, X. Chen, L. Wang, Z. Ye, Carbon 137 (2018) 368–378.
[76] E. Fleming, I. Kholmanov, L. Shi, Carbon 136 (2018) 380–386.
[77] Z. Wang, H.Y. Yue, Z.M. Yu, S. Huang, X. Gao, B. Wang, S.S. Song, E.H. Guan, W.Q. Wang, H.J. Zhang, Ionics 24 (2018) 1813–1823.
[78] G. Ning, Z. Fan, G. Wang, J. Gao, W. Qian, F. Wei, Chem. Commun. 47 (2011) 5976–5978.
[79] J. Chen, Y. Wen, Y. Guo, B. Wu, L. Huang, Y. Xue, D. Geng, D. Wang, G. Yu, Y. Liu, J. Am. Chem. Soc. 133 (2011) 17548–17551.
[80] J. Sun, T. Gao, X. Song, Y. Zhao, Y. Lin, H. Wang, D. Ma, Y. Chen, W. Xiang, J. Wang, Y. Zhang, Z. Liu, J. Am. Chem. Soc. 136 (2014) 6574–6577.
[81] P. Trinsoutrot, H. Vergnes, B. Caussat, Mater. Sci. Eng. B 179 (2014) 12–16.
[82] Y. Ito, W. Cong, T. Fujita, Z. Tang, M. Chen, Angew. Chem. Int. Ed. 54 (2015) 2131–2136.
[83] Y. Ito, Y. Tanabe, J. Han, T. Fujita, K. Tanigaki, M. Chen, Adv. Mater. 27 (2015) 4302–4307.
[84] R. Mo, D. Rooney, K. Sun, H.Y. Yang, Nat. Commun. 8 (2017) 13949.
[85] C. Li, Y. Hu, M. Yu, Z. Wang, W. Zhao, P. Liu, Y. Tong, X. Lu, RSC Adv. 4 (2014) 51878–51883.
[86] C.N.R. Rao, K. Gopalakrishnan, A. Govindaraj, Nano Today 9 (2014) 324–343.
[87] W. Zhang, C. Xu, C. Ma, G. Li, Y. Wang, K. Zhang, F. Li, C. Liu, H.M. Cheng, Y. Du, N. Tang, W. Ren,Adv. Mater. 29 (2017), 1701677.
[88] J.R. Miller, R.A. Outlaw, B.C. Holloway, Science 329 (2010) 1637–1639.
[89] G. Ren, M.N.F. Hoque, J. Liu, J. Warzywoda, Z. Fan, Nano Energy 21 (2016) 162–171.
[90] H. Ren, M. Tang, B. Guan, K. Wang, J. Yang, F. Wang, M. Wang, J. Shan, Z. Chen, D. Wei, H. Peng, Z. Liu,Adv. Mater. 29 (2017), 1702590.
[91] S. Yang, Z. Bo, H. Yang, X. Shuai, H. Qi, X. Li, J. Yan, K. Cen, Ind. Eng. Chem. Res. 57 (2018) 15291–15300.
[92] M.C. Wang, J. Leem, P. Kang, J. Choi, P. Knapp, K. Yong, S. Nam,2D Materials 4 (2017), 022002.
[93] W. Chen, X. Gui, B. Liang, M. Liu, Z. Lin, Y. Zhu, Z. Tang, ACS Appl. Mater. Interfaces 8 (2016) 10977–10984.
[94] Z. Pan, N. Liu, L. Fu, Z. Liu, J. Am. Chem. Soc. 133 (2011) 17578–17581.
[95] J. Zang, S. Ryu, N. Pugno, Q. Wang, Q. Tu, M.J. Buehler, X. Zhao, Nat. Mater. 12 (2013) 321–325.
[96] H. Chen, Y. Xu, L. Bai, Y. Jiang, J. Zhang, C. Zhao, T. Li, H. Yu, G. Song, N. Zhang, Q. Gan,Adv. Mater. Technol. 2 (2017), 1700044.
[97] J. Choi, H.J. Kim, M.C. Wang, J. Leem, W.P. King, S. Nam, Nano Lett. 15 (2015) 4525–4531.
[98] M. Loeblein, S.H. Tsang, M. Pawlik, E.J.R. Phua, H. Yong, X.W. Zhang, C.L. Gan, E.H.T. Teo, ACS Nano 11 (2017) 2033–2044.
[99] H. Zhou, Y. Wang, R. He, F. Yu, J. Sun, F. Wang, Y. Lan, Z. Ren, S. Chen, Nano Energy 20 (2016) 29–36.
[100] J. Yin, X. Li, J. Zhou, W. Guo, Nano Lett. 13 (2013) 3232–3236.
[101] Y. Song, B. Li, S. Yang, G. Ding, C. Zhang, X. Xie, Sci. Rep. 5 (2015) 10337.
[102] X. Xu, Q. Zhang, M. Hao, Y. Hu, Z. Lin, L. Peng, T. Wang, X. Ren, C. Wang, Z. Zhao, C. Wan, H. Fei, L. Wang, J. Zhu, H. Sun, W. Chen, T. Du, B. Deng, G.J. Cheng, I. Shakir, C. Dames, T.S. Fisher, X. Zhang, H. Li, Y. Huang, X. Duan, Science 363 (2019) 723–727.
[103] Y. Xue, P. Dai, M. Zhou, X. Wang, A. Pakdel, C. Zhang, Q. Weng, T. Takei, X. Fu, Z.I. Popov, ACS Nano 11 (2016) 558–568.
[104] M. Maleki, M. Shokouhimehr, H. Karimian, A. Beitollahi, RSC Adv. 6 (2016) 51426–51434.
[105] H. Zhou, F. Yu, Y. Huang, J. Sun, Z. Zhu, R.J. Nielsen, R. He, J. Bao, W.A. Goddard III, S. Chen, Nat. Commun. 7 (2016) 12765.
[106] H. Zhou, F. Yu, J. Sun, H. Zhu, I.K. Mishra, S. Chen, Z. Ren, Nano Lett. 16 (2016) 7604–7609.
[107] J.S. Lee, H.J. Ahn, J.C. Yoon, J.H. Jang, Phys. Chem. Chem. Phys. 14 (2012) 7938–7943.
[108] X. Xiao, T.E. Beechem, M.T. Brumbach, T.N. Lambert, D.J. Davis, J.R. Michael, C.M. Washburn, J. Wang, S.M. Brozik, D.R. Wheeler, D.B. Burckel, R. Polsky, ACS Nano 6 (2012) 3573–3579.
[109] Y. Xue, P. Dai, X. Jiang, X. Wang, C. Zhang, D. Tang, Q. Weng, X. Wang, A. Pakdel, C. Tang, J. Mater. Chem. A 4 (2016) 1469–1478.
[110] Y.H. Chang, C.T. Lin, T.Y. Chen, C.L. Hsu, Y.H. Lee, W. Zhang, K.H. Wei, L.J. Li, Adv. Mater. 25 (2013) 756–760.
[111] X. Cao, Y. Shi, W. Shi, X. Rui, Q. Yan, J. Kong, H. Zhang, Small 9 (2013) 3433–3438.
[112] Q. Zhang, S. Tan, R.G. Mendes, Z. Sun, Y. Chen, X. Kong, Y. Xue, M.H. Rummeli, X. Wu, S. Chen, L. Fu, Adv. Mater. 28 (2016) 2616–2623.
[113] M.A. Worsley, S.J. Shin, M.D. Merrill, J. Lenhardt, A.J. Nelson, L.Y. Woo, A.E. Gash, T.F. Baumann, C.A. Orme, ACS Nano 9 (2015) 4698–4705.
[114] H. Long, L. Chan, A. Harley-Trochimczyk, L.E. Luna, Z. Tang, T. Shi, A. Zettl, C. Carraro, M.A. Worsley, R. Maboudian,Adv. Mater. Interfaces 4 (2017), 1700217.
[115] M.M. Gudarzi, Langmuir 32 (2016) 5058–5068.
[116] Y. Xu, K. Sheng, C. Li, G. Shi, ACS Nano 4 (2010) 4324–4330.
[117] Y. Zou, I.A. Kinloch, R.A.W. Dryfe, J. Mater. Chem. A 2 (2014) 19495–19499.
[118] C.K. Chua, M. Pumera, Chem. Soc. Rev. 43 (2014) 291–312.
[119] C.-J. Shih, S. Lin, R. Sharma, M.S. Strano, D. Blankschtein, Langmuir 28 (2012) 235–241.
[120] H. Ha, K. Shanmuganathan, C.J. Ellison, ACS Appl. Mater. Interfaces 7 (2015) 6220–6229.
[121] X. Hu, W. Xu, L. Zhou, Y. Tan, Y. Wang, S. Zhu, J. Zhu,Adv. Mater. 29 (2017), 1604031.
[122] J. Abraham, K.S. Vasu, C.D. Williams, K. Gopinadhan, Y. Su, C.T. Cherian, J. Dix, E. Prestat, S.J. Haigh, I.V. Grigorieva, P. Carbone, A.K. Geim, R.R. Nair, Nat. Nanotechnol. 12 (2017) 546–550.
[123] X. Tang, H. Zhou, Z. Cai, D. Cheng, P. He, P. Xie, D. Zhang, T. Fan, ACS Nano 12 (2018) 3502–3511.
[124] Y. Ling, X. Zhuang, Z. Xu, Y. Xie, X. Zhu, Y. Xu, B. Sun, J. Lin, Y. Zhang, Z. Yan, ACS Nano 12 (2018) 12456–12463.
[125] J. Wang, J. Liu, D. Chao, J. Yan, J. Lin, Z.X. Shen, Adv. Mater. 26 (2014) 7162–7169.
[126] T.T. Shan, S. Xin, Y. You, H.P. Cong, S.H. Yu, A. Manthiram, Angew. Chem. Int. Ed. 55 (2016) 12783–12788.
[127] Y. Guo, Y. Zhang, Y. Wang, D. Zhang, Y. Lu, R. Luo, Y. Wang, X. Liu, J.-K. Kim, Y. Luo, Electrochim. Acta 296 (2019) 989–998.
[128] P.T. Gomathi, P. Sahatiya, S. Badhulika,Adv. Funct. Mater. 27 (2017), 1701611.
[129] X. Liu, J.-Z. Zhang, K.-J. Huang, P. Hao, Chem. Eng. J. 302 (2016) 437–445.
[130] K. Hu, J. Zhou, Z. Yi, C. Ye, H. Dong, K. Yan, Appl. Surf. Sci. 465 (2019) 351–356.
[131] J. He, Q. Li, Y. Chen, C. Xu, K. Zhou, X. Wang, W. Zhang, Y. Li, Carbon 114 (2017) 111–116.
[132] H.-C. Chen, Y.-C. Lin, Y.-L. Chen, C.-J. Chen, ACS Appl. Energy Mater. 2 (2019) 459–467.
[133] P.S. Owuor, O.-K. Park, C.F. Woellner, A.S. Jalilov, S. Susarla, J. Joyner, S. Ozden, L. Duy, R. Villegas Salvatierra, R. Vajtai, ACS Nano 11 (2017) 8944–8952.
[134] J. He, P. Li, W. Lv, K. Wen, Y. Chen, W. Zhang, Y. Li, W. Qin, W. He, Electrochim. Acta 215 (2016) 12–18.
[135] Y. Ma, Y. Yue, H. Zhang, F. Cheng, W. Zhao, J. Rao, S. Luo, J. Wang, X. Jiang, Z. Liu, N. Liu, Y. Gao, ACS Nano 12 (2018) 3209–3216.
[136] S. Zhao, H.-B. Zhang, J.-Q. Luo, Q.-W. Wang, B. Xu, S. Hong, Z.-Z. Yu, ACS Nano 12 (2018) 11193–11202.
[137] C. Liu, X. Zhao, S. Wang, Y. Zhang, W. Ge, J. Li, J. Cao, J. Tao, X. Yang, ACS Appl. Energy Mater. 2 (2019) 4458–4463.
[138] X. Yang, C. Cheng, Y. Wang, L. Qiu, D. Li, Science 341 (2013) 534.
[139] J. Huang, M. Chen, X. Li, X. Zhang, L. Lin, W. Liu, Y. Liu, Electrochim. Acta 300 (2019) 235–241.
[140] Z. Niu, J. Chen, H.H. Hng, J. Ma, X. Chen, Adv. Mater. 24 (2012) 4144–4150.
[141] S.C. Yoo, Y.K. Park, C. Park, H. Ryu, S.H. Hong,Adv. Funct. Mater. 28 (2018), 1805948.
[142] M.-Q. Zhao, X. Xie, C.E. Ren, T. Makaryan, B. Anasori, G. Wang, Y. Gogotsi,Adv. Mater. 29 (2017), 1702410.
[143] Y. Yue, N. Liu, W. Liu, M. Li, Y. Ma, C. Luo, S. Wang, J. Rao, X. Hu, J. Su, Z. Zhang, Q. Huang, Y. Gao, Nano Energy 50 (2018) 79–87.
[144] Z. Wan, Y. Jiao, X. Ouyang, L. Chang, X. Wang, Appl. Mater. Today 9 (2017) 551–559.
[145] Y. Zhou, Y. Wang, T. Liu, G. Xu, G. Chen, H. Li, L. Liu, Q. Zhuo, J. Zhang, C. Yan, Sci. Rep. 7 (2017) 45065.
[146] M. Hu, Z. Li, H. Zhang, T. Hu, C. Zhang, Z. Wu, X. Wang, ChemComm 51 (2015) 13531–13533.
[147] L. Jing, H. Li, R.Y. Tay, B. Sun, S.H. Tsang, O. Cometto, J. Lin, E.H.T. Teo, A.I.Y. Tok, ACS Nano 11 (2017) 3742–3751.
[148] S. Nagarajan, H. Belaid, C. Pochat-Bohatier, C. Teyssier, I. Iatsunskyi, E. Coy, S. Balme, D. Cornu, P. Miele, N.S. Kalkura, ACS Appl. Mater. Interfaces 9 (2017) 33695–33706.
[149] Q. Li, L. Chen, M.R. Gadinski, S. Zhang, G. Zhang, H.U. Li, E. Iagodkine, A. Haque, L.-Q. Chen, T.N. Jackson, Q. Wang, Nature 523 (2015) 576–579.
[150] Y.-Z. Zhang, K.H. Lee, D.H. Anjum, R. Sougrat, Q. Jiang, H. Kim, H.N. Alshareef, Sci. Adv. 4 (2018), eaat0098.
[151] X. Hu, Y. Li, G. Zeng, J. Jia, H. Zhan, Z. Wen, ACS Nano 12 (2018) 1592–1602.
[152] H. Qiu, X. Dong, B. Sana, T. Peng, D. Paramelle, P. Chen, S. Lim, ACS Appl. Mater. Interfaces 5 (2013) 782–787.
[153] Q. Chang, L. Huang, J. Wang, Z. Ma, P. Li, Y. Yan, J. Zhu, S. Xu, L. Shen, Q. Chen, Q. Yu, W. Shi, Carbon 85 (2015) 185–193.
[154] J. Liu, L. Zhang, H.B. Wu, J. Lin, Z. Shen, X.W. Lou, Energy Environ. Sci. 7 (2014) 3709–3719.
[155] X. Xia, D. Chao, Z. Fan, C. Guan, X. Cao, H. Zhang, H.J. Fan, Nano Lett. 14 (2014) 1651–1658.
[156] Z. Chen, C. Xu, C. Ma, W. Ren, H.M. Cheng, Adv. Mater. 25 (2013) 1296–1300.
[157] L. Xiu, Z. Wang, M. Yu, X. Wu, J. Qiu, ACS Nano 12 (2018) 8017–8028.
[158] M.T. Pettes, H. Ji, R.S. Ruoff, L. Shi, Nano Lett. 12 (2012) 2959–2964.
[159] I. Kholmanov, J. Kim, E. Ou, R.S. Ruoff, L. Shi, ACS Nano 9 (2015) 11699–11707.
[160] A. Nieto, B. Boesl, A. Agarwal, Carbon 85 (2015) 299–308.
[161] X. Tong, S. Chen, C. Guo, X. Xia, X.Y. Guo, ACS Appl. Mater. Interfaces 8 (2016) 28274–28282.

[162] X. Wu, S. Li, B. Wang, J. Liu, M. Yu, New J. Chem. 41 (2017) 115–125.
[163] T. Maiyalagan, X. Dong, P. Chen, X. Wang, J. Mater. Chem. 22 (2012) 5286–5290.
[164] S. Sattayasamitsathit, Y. Gu, K. Kaufmann, W. Jia, X. Xiao, M. Rodriguez, S. Minteer, J. Cha, D.B. Burckel, C. Wang, R. Polsky, J. Wang, J. Mater. Chem. A 1 (2013) 1639–1645.
[165] Y.-C. Yong, X.-C. Dong, M.B. Chan-Park, H. Song, P. Chen, ACS Nano 6 (2012) 2394–2400.
[166] B. Tang, G. Hu, H. Gao, Z. Shi, J. Power Sources 234 (2013) 60–68.
[167] J. Zhi, H. Cui, A. Chen, Y. Xie, F. Huang, J. Power Sources 281 (2015) 404–410.
[168] P. Zhang, L. Li, D. Nordlund, H. Chen, L. Fan, B. Zhang, X. Sheng, Q. Daniel, L. Sun, Nat. Commun. 9 (2018) 381.
[169] X. Guo, J. Ji, Q. Jiang, L. Zhang, Z. Ao, X. Fan, S. Wang, Y. Li, F. Zhang, G. Zhang, ACS Appl. Mater. Interfaces 9 (2017) 30591–30598.
[170] Y. Tong, X. Yu, G. Shi, Phys. Chem. Chem. Phys. 19 (2017) 4821–4826.
[171] K.-R. Lee, S.H. Jang, I. Jung, Carbon 127 (2018) 13–20.
[172] W. Wang, S. Guo, M. Penchev, I. Ruiz, K.N. Bozhilov, D. Yan, M. Ozkan, C.S. Ozkan, Nano Energy 2 (2013) 294–303.
[173] X. Wang, Y. Zhang, C. Zhi, X. Wang, D. Tang, Y. Xu, Q. Weng, X. Jiang, M. Mitome, D. Golberg, Y. Bando, Nat. Commun. 4 (2013) 2905.
[174] C. Wu, S. Deng, H. Wang, Y. Sun, J. Liu, H. Yan, ACS Appl. Mater. Interfaces 6 (2014) 1106–1112.
[175] J. Ji, L.L. Zhang, H. Ji, Y. Li, X. Zhao, X. Bai, X. Fan, F. Zhang, R.S. Ruoff, ACS Nano 7 (2013) 6237–6243.
[176] X.-C. Dong, H. Xu, X.-W. Wang, Y.-X. Huang, M.B. Chan-Park, H. Zhang, L.-H. Wang, W. Huang, P. Chen, ACS Nano 6 (2012) 3206–3213.
[177] T. Yin, W. Zhang, Y. Yin, Y. Yan, K. Zhan, J. Yang, B. Zhao, J. Mater. Sci. Mater. Electron. 28 (2017) 7884–7891.
[178] G. Xiong, P. He, D. Wang, Q. Zhang, T. Chen, T.S. Fisher, Adv. Funct. Mater. 26 (2016) 5460–5470.
[179] K. Chi, Z. Zhang, Q. Lv, C. Xie, J. Xiao, F. Xiao, S. Wang, ACS Appl. Mater. Interfaces 9 (2017) 6044–6053.
[180] T.M. Masikhwa, M.J. Madito, A. Bello, J.K. Dangbegnon, N. Manyala, J. Colloid Interface Sci. 488 (2017) 155–165.
[181] Z. Kang, Y. Li, Y. Yu, Q. Liao, Z. Zhang, H. Guo, S. Zhang, J. Wu, H. Si, X. Zhang, Y. Zhang, J. Mater. Sci. 53 (2018) 10292–10301.
[182] J. Pedrós, A. Boscá, J. Martínez, S. Ruiz-Gómez, L. Pérez, V. Barranco, F. Calle, J. Power Sources 317 (2016) 35–42.
[183] S.K. Balasingam, M. Lee, B.H. Kim, J.S. Lee, Y. Jun, Dalton Trans. 46 (2017) 2122–2128.
[184] Y. Yue, N. Liu, Y. Ma, S. Wang, W. Liu, C. Luo, H. Zhang, F. Cheng, J. Rao, X. Hu, J. Su, Y. Gao, ACS Nano 12 (2018) 4224–4232.
[185] C. Sha, B. Lu, H. Mao, J. Cheng, X. Pan, J. Lu, Z. Ye, Carbon 99 (2016) 26–34.
[186] D. Chao, X. Xia, J. Liu, Z. Fan, C.F. Ng, J. Lin, H. Zhang, Z.X. Shen, H.J. Fan, Adv. Mater. 26 (2014) 5794–5800.
[187] N. Li, Z. Chen, W. Ren, F. Li, H.-M. Cheng, Proc. Natl. Acad. Sci. U. S. A. 109 (2012) 17360–17365.
[188] G. Hu, C. Xu, Z. Sun, S. Wang, H.M. Cheng, F. Li, W. Ren, Adv. Mater. 28 (2016) 1603–1609.
[189] J. He, Y. Chen, W. Lv, K. Wen, P. Li, F. Qi, Z. Wang, W. Zhang, Y. Li, W. Qin, W. He, J. Power Sources 327 (2016) 474–480.
[190] J. Zhang, P. Li, Z. Wang, J. Qiao, D. Rooney, W. Sun, K. Sun, J. Mater. Chem. A 3 (2015) 1504–1510.
[191] X. Yu, B. Wang, D. Gong, Z. Xu, B. Lu,Adv. Mater. 29 (2017), 1604118.
[192] J. Xiang, D. Dong, F. Wen, J. Zhao, X. Zhang, L. Wang, Z. Liu, J. Alloys Compd. 660 (2016) 11–16.
[193] D. Zhang, S. Wang, Y. Ma, S. Yang, J. Energy Chem. 27 (2018) 128–145.
[194] N. Zhang, X. Yan, Y. Huang, J. Li, J. Ma, D.H.L. Ng, Langmuir 33 (2017) 8899–8905.
[195] J. Shao, H. Zhou, M. Zhu, J. Feng, A. Yuan, J. Alloys Compd. 768 (2018) 1049–1057.
[196] J. Deng, L. Chen, Y. Sun, M. Ma, L. Fu, Carbon 92 (2015) 177–184.
[197] B. Wang, S. Li, X. Wu, J. Liu, W. Tian, Phys. Chem. Chem. Phys. 18 (2016) 908–915.
[198] X. Wang, Q. Chen, P. Zhao, M. Wang, RSC Adv. 8 (2018) 33717–33727.
[199] H. Ji, L. Zhang, M.T. Pettes, H. Li, S. Chen, L. Shi, R. Piner, R.S. Ruoff, Nano Lett. 12 (2012) 2446–2451.
[200] J. Ji, H. Ji, L.L. Zhang, X. Zhao, X. Bai, X. Fan, F. Zhang, R.S. Ruoff, Adv. Mater. 25 (2013) 4673–4677.
[201] X. Ma, X. Liu, J. Zhao, J. Hao, C. Chi, X. Liu, Y. Li, S. Liu, K. Zhang, New J. Chem. 41 (2017) 588–593.
[202] A.P. Cohn, L. Oakes, R. Carter, S. Chatterjee, A.S. Westover, K. Share, C.L. Pint, Nanoscale 6 (2014) 4669–4675.
[203] J. Ren, Z. Wang, F. Yang, R.-P. Ren, Y.-K. Lv, Electrochim. Acta 267 (2018) 133–140.
[204] X. Zhang, R. Lv, A. Wang, W. Guo, X. Liu, J. Luo, Angew. Chem. Int. Ed. 57 (2018) 15028–15033.
[205] Z. Ma, X. Zhou, W. Deng, D. Lei, Z. Liu, ACS Appl. Mater. Interfaces 10 (2018) 3634–3643.
[206] A. Eftekhari, Sustain. Energy Fuels 1 (2017) 2053–2060.
[207] Y. Wu, Z. Wang, X. Liu, X. Shen, Q. Zheng, Q. Xue, J.K. Kim, ACS Appl. Mater. Interfaces 9 (2017) 9059–9069.
[208] X. Sun, X. Liu, X. Shen, Y. Wu, Z. Wang, J.-K. Kim, Compos. Part A: Appl. Sci. Manuf. 92 (2017) 190–197.
[209] H. Ji, D.P. Sellan, M.T. Pettes, X. Kong, J. Ji, L. Shi, R.S. Ruoff, Energy Environ. Sci. 7 (2014) 1185–1192.
[210] J. Yang, G.-Q. Qi, R.-Y. Bao, K. Yi, M. Li, L. Peng, Z. Cai, M.-B. Yang, D. Wei, W. Yang, Energy Storage Mater. 13 (2018) 88–95.
[211] H. Fang, Y. Zhao, Y. Zhang, Y. Ren, S.L. Bai, ACS Appl. Mater. Interfaces 9 (2017) 26447–26459.
[212] Y. Wu, X. Sun, W. Wu, X. Liu, X. Lin, X. Shen, Z. Wang, R.K.Y. Li, Z. Yang, K.-T. Lau, J.-K. Kim, Compos. Part A: Appl. Sci. Manuf. 102 (2017) 391–399.
[213] Y. Qiu, J. Liu, Y. Lu, R. Zhang, W. Cao, P. Hu, ACS Appl. Mater. Interfaces 8 (2016) 18496–18504.
[214] X. Dong, X. Wang, L. Wang, H. Song, H. Zhang, W. Huang, P. Chen, ACS Appl. Mater. Interfaces 4 (2012) 3129–3133.
[215] X. Dong, Y. Ma, G. Zhu, Y. Huang, J. Wang, M.B. Chan-Park, L. Wang, W. Huang, P. Chen, J. Mater. Chem. 22 (2012) 17044.
[216] X. Feng, Y. Zhang, J. Zhou, Y. Li, S. Chen, L. Zhang, Y. Ma, L. Wang, X. Yan, Nanoscale 7 (2015) 2427–2432.
[217] X. Cao, Z. Zeng, W. Shi, P. Yep, Q. Yan, H. Zhang, Small 9 (2013) 1703–1707.
[218] I. Shackery, U. Patil, A. Pezeshki, N.M. Shinde, S. Kang, S. Im, S.C. Jun, Electrochim. Acta 191 (2016) 954–961.
[219] X. Gao, H. Yue, S. Huang, X. Lin, X.P.A. Gao, B. Wang, L. Yao, W. Wang, E. Guo, J. Electroanal. Chem. 808 (2018) 189–194.
[220] C.C. Kung, P.Y. Lin, F.J. Buse, Y. Xue, X. Yu, L. Dai, C.C. Liu, Biosens. Bioelectron. 52 (2014) 1–7.
[221] I. Shackery, U. Patil, M.-J. Song, J.S. Sohn, S. Kulkarni, S. Some, S.C. Lee, M.S. Nam, W. Lee, S.C. Jun, Electroanalysis 27 (2015) 2363–2370.
[222] F. Xi, D. Zhao, X. Wang, P. Chen, Electrochem. Commun. 26 (2013) 81–84.
[223] P. Si, X.-C. Dong, P. Chen, D.-H. Kim, J. Mater. Chem. B 1 (2013) 110–115.
[224] W. Xu, N. Mao, J. Zhang, Small 9 (2013) 1206–1224.
[225] J. Leem, M.C. Wang, P. Kang, S. Nam, Nano Lett. 15 (2015) 7684–7690.
[226] C. Srichan, M. Ekpanyapong, M. Horprathum, P. Eiamchai, N. Nuntawong, D. Phokharatkul, P. Danvirutai, E. Bohez, A. Wisitsoraat, A. Tuantranont, Sci. Rep. 6 (2016) 23733.
[227] A.A. Khaleed, A. Bello, J.K. Dangbegnon, M.J. Madito, F.U. Ugbo, A.A. Akande, B.P. Dhonge, F. Barzegar, D.Y. Momodu, B.W. Mwakikunga, N. Manyala, J. Mater. Sci. 52 (2016) 2035–2044.
[228] F. Yavari, Z. Chen, A.V. Thomas, W. Ren, H.M. Cheng, N. Koratkar, Sci. Rep. 1 (2011) 166.
[229] W. Yuan, K. Yang, H. Peng, F. Li, F. Yin, J. Mater. Chem. A 6 (2018) 18116–18124.
[230] W. Li, J. Guo, D. Fan,Adv. Mater. Technol. 2 (2017), 1700070.
[231] S.J. Kim, S. Mondal, B.K. Min, C.G. Choi, ACS Appl. Mater. Interfaces 10 (2018) 36377–36384.
[232] F. Pan, S.-M. Chen, Y. Li, Z. Tao, J. Ye, K. Ni, H. Yu, B. Xiang, Y. Ren, F. Qin, S.-H. Yu, Y. Zhu,Adv. Funct. Mater. 28 (2018), 1803221.
[233] Y. Pang, H. Tian, L. Tao, Y. Li, X. Wang, N. Deng, Y. Yang, T.L. Ren, ACS Appl. Mater. Interfaces 8 (2016) 26458–26462.
[234] X. Dong, J. Chen, Y. Ma, J. Wang, M.B. Chan-Park, X. Liu, L. Wang, W. Huang, P. Chen, Chem. Commun. 48 (2012) 10660–10662.
[235] X. Gao, X. Wang, X. Ouyang, C. Wen, Sci. Rep. 6 (2016) 27207.
[236] J. Bong, T. Lim, K. Seo, C.A. Kwon, J.H. Park, S.K. Kwak, S. Ju, Sci. Rep. 5 (2015) 14321.
[237] E. Singh, Z. Chen, F. Houshmand, W. Ren, Y. Peles, H.M. Cheng, N. Koratkar, Small 9 (2013) 75–80.
[238] S. Yu, X. Wang, H. Pang, R. Zhang, W. Song, D. Fu, T. Hayat, X. Wang, Chem. Eng. J. 333 (2018) 343–360.
[239] X. Li, B. Zhu, J. Zhu, Carbon 146 (2019) 320–328.
[240] X. Zhou, F. Zhao, Y. Guo, Y. Zhang, G. Yu, Energy Environ. Sci. 11 (2018) 1985–1992.
[241] W. Li, Z. Li, K. Bertelsmann, D.E. Fan,Adv. Mater. 31 (2019), 1900720.
[242] Q. Yao, J. Jing, Q. Zeng, T.L. Lu, Y. Liu, X. Zheng, Q. Chen, ACS Appl. Mater. Interfaces 9 (2017) 39962–39970.
[243] C. Gautam, D. Chakravarty, A. Gautam, C.S. Tiwary, C.F. Woellner, V.K. Mishra, N. Ahmad, S. Ozden, S. Jose, S. Biradar, ACS Omega 3 (2018) 6013–6021.
[244] E. Krueger, A.N. Chang, D. Brown, J. Eixenberger, R. Brown, S. Rastegar, K.M. Yocham, K.D. Cantley, D. Estrada, ACS Biomater. Sci. Eng. 2 (2016) 1234–1241.
[245] M.-Y. Li, C.-H. Chen, Y. Shi, L.-J. Li, Mater. Today 19 (2016) 322–335.
[246] M.J. Crane, M.B. Lim, X. Zhou, P.J. Pauzauskie, Microsyst. Nanoeng. 3 (2017) 17032.
[247] T. Cheng, B. Yu, L. Cao, H. Tan, X. Li, X. Zheng, W. Li, Z. Ren, J. Bai, J. Colloid Interface Sci. 501 (2017) 1–10.
[248] H. Chu, F. Zhang, L. Pei, Z. Cui, J. Shen, M. Ye, J. Alloys Compd. 767 (2018) 583–591.
[249] Z. Ma, Y. Wang, Y. Yang, M. Yousaf, M. Zou, A. Cao, R.P.S. Han, RSC Adv. 6 (2016) 30098–30105.
[250] Y. Wang, D. Kong, W. Shi, B. Liu, G.J. Sim, Q. Ge, H.Y. Yang,Adv. Energy Mater. 6 (2016), 1601057.
[251] W.S.V. Lee, E. Peng, T.A.J. Loh, X. Huang, J.M. Xue, Nanoscale 8 (2016) 8042–8047.

Weigu Li received his Ph.D. degree in Mechanical Engineering with focus on Materials Engineering from the University of Texas at Austin in 2019, and B.S. degree in Material Chemistry from the Department of Materials Science and Engineering and Lu Jiaxi Talent Program in Chemistry at the University of Science and Technology of China (USTC) in 2013. His research interest lies in the structural design and manufacturing of 3D porous monolithic superstructures for flexible self-powered electronics (strain sensors, nanomotors), energy conversion and storage devices (supercapacitors, water splitting), and water purification systems (solar steaming, heavy metal removal, and crude oil absorption).

Yun Huang has been a Ph.D. student in the Materials Science and Engineering Program at the University of Texas at Austin since 2016. She received her master degree in Condensed Matter Physics from the University of Chinese Academy of Sciences (UCAS) and bachelor's degree in Materials Science and Engineering from the Dalian University of Technology (DUT) in 2016 and 2013, respectively. Her current research focuses on the applications of novel 2D materials in micro/nanorobotics and energy devices.

Yifei Liu is a Ph.D. student in the Material Science and Engineering program at the University of Texas at Austin. He received his B.S. in Material Chemistry from the University of Science and Technology of China in 2018. His research interest includes design and synthesis of 3D porous materials for electrochemical catalysis and energy conversion.

Marshall C. Tekell received his B.S. in Chemical Engineering and B.A. in Plan II Honors from the University of Texas at Austin in 2019 under the supervision of Professor Donglei Fan. His research interests include the synthesis and characterization of 2D materials for energy storage and conversion applications. In September 2019, he begins in a Ph.D. program in Chemical Engineering at Columbia University.

Donglei (Emma) Fan is an Associate Professor in the Department of Mechanical Engineering at the University of Texas at Austin. She holds the Robert & Jane Mitchell Endowed Faculty Fellowship in Engineering. She received her bachelor's degree in Chemistry in the Department of Intensive Instruction, an honor program for talented undergraduates, from Nanjing University (1999), and doctorate (2007) degrees in Materials Science and Engineering from the Johns Hopkins University. Her research focuses on manufacturing, manipulation, robotization, and assembly of micro/nanostructured materials via understanding and exploiting fundamental materials science, physics, and chemistry. The applications include robotics, biochemical sensing, flexible 3D porous catalyts, solar steaming for water treatment, and self-powered systems. Dr. Fan is a particularly interested in the investigation of innovative mechanisms for programmably manufacturing 3D nanoporous materials, highly important for energy and environmental devices and soft robotics. Dr. Fan received the National Science Foundation CAREER Award in 2012.